

MICROSTRUCTURAL ANALYSIS OF CALCIUM-ALUMINUM-RICH INCLUSIONS

by

Diana Bolser

---

A Thesis Submitted to the Faculty of the

DEPARTMENT OF CHEMISTRY AND BIOCHEMISTRY

In Partial Fulfillment of the Requirements

For the Degree of

MASTER OF SCIENCE  
WITH A MAJOR IN CHEMISTRY

In the Graduate College

THE UNIVERSITY OF ARIZONA

2014

## STATEMENT BY AUTHOR

This thesis has been submitted in partial fulfillment of requirements for an advanced degree at the University of Arizona and is deposited in the University Library to be made available to borrowers under rules of the Library.

Brief quotations from this thesis are allowable without special permission, provided that an accurate acknowledgement of the source is made. Requests for permission for extended quotation from or reproduction of this manuscript in whole or in part may be granted by the head of the major department or the Dean of the Graduate College when in his or her judgment the proposed use of the material is in the interests of scholarship. In all other instances, however, permission must be obtained from the author.

SIGNED: Diana Bolser

## APPROVAL BY THESIS DIRECTOR

This thesis has been approved on the date shown below:

\_\_\_\_\_  
Lucy Ziurys  
Professor of Chemistry and Biochemistry

November 24, 2014  
Date

## ACKNOWLEDGMENTS

I would like to express my deepest gratitude to my advisor, Professor Thomas Zega, for his excellent guidance and for the opportunity to contribute my research to the field of cosmochemistry. I also want to thank my fellow PMRG'ers Michelle Thompson, Dr. Ken Domanik, and Dolores Hill for their support. Research funded in part by NESSF grant NNX14AO56H.

## TABLE OF CONTENTS

LIST OF FIGURES .....	5
ABSTRACT.....	6
CHAPTER 1 BACKGROUND .....	7
1.1 SCOPE OF THE THESIS.....	7
1.2 METEORITE CLASSIFICATION .....	7
1.3 CALCIUM-ALUMINUM-RICH INCLUSIONS.....	8
CHAPTER 2 ANALYTICAL TECHNIQUES .....	11
2.1 ELECTRON BACKSCATTER DIFFRACTION .....	11
2.2 TRANSMISSION ELECTRON MICROSCOPY .....	12
2.3 FOCUSED-ION-BEAM SCANNING ELECTRON MICROSCOPY .....	14
2.4 SCANNING TRANSMISSION X-RAY MICROSCOPY.....	15
2.5 ELECTRON MICROPROBE.....	16
2.6 ENERGY DISPERSIVE X-RAY MICROSCOPY .....	18
CHAPTER 3 MICROSTRUCTURAL ANALYSIS OF WARK-LOVERING RIMS.....	25
3.1 INTRODUCTION .....	25
3.2 SAMPLES AND METHODOLOGY.....	27
3.3 RESULTS .....	29
3.3.1 PETROGRAPHY AND MINERALOGY.....	29
3.3.2 EBSD ANALYSIS.....	29
3.3.3 TEM CROSS-SECTIONAL ANALYSIS .....	31
3.3.4 DENSITY FUNCTIONAL THEORY SIMULATIONS .....	32
3.4 DISCUSSION.....	33
3.5 CONCLUSIONS.....	38
CHAPTER 4 DEVELOPMENT OF A $fO_2$ BAROMETER.....	46
4.1 INTRODUCTION TO OXYGEN FUGACITY.....	46
4.2 LABORATORY SYNTHESIS OF PEROVSKITE .....	47
4.3 DETERMINATION OF TI VALENCE STATE .....	48
4.3.1 APPLICATION TO METEORITIC PEROVSKITE .....	50
CHAPTER 5 SUMARY AND FUTURE WORK.....	57
REFERENCES .....	58

## LIST OF FIGURES

Fig. 2.1 Kikuchi diffraction pattern formation.....	19
Fig. 2.2 Kikuchi diffraction pattern of diopside .....	20
Fig. 2.3 Beam-specimen interactions in a TEM .....	21
Fig. 2.4 Optical diagram of a TEM.....	22
Fig. 2.5 Step-by-step illustration of FIB lift-out.....	23
Fig. 2.6 X-ray absorption in a transition metal atom .....	24
Fig. 3.1 Backscattered electron images of AX30 .....	39
Fig. 3.2 Backscattered electron image of TS25 .....	40
Fig. 3.3 EBSD data from AX30.....	41
Fig. 3.4 EBSD data from TS25.....	42
Fig. 3.5 TEM data from AX30.....	43
Fig. 3.6 TEM data from TS25.....	44
Fig. 3.7 Schematic model depicting WLR growth .....	45
Fig. 4.1 Gas-mixing furnace .....	52
Fig. 4.2 Temperature profile of the furnace.....	53
Fig. 4.3 Ti L <sub>2,3</sub> electron energy loss spectra of Ti oxides.....	54
Fig. 4.4 Bright field TEM image of AX30 .....	55
Fig. 4.5 Ti L <sub>2,3</sub> XANES spectra of perovskite.....	56

## ABSTRACT

Refractory materials are among the building blocks of our solar system and their chemistry and structure hold clues to understanding our origins. In this thesis I present a multifaceted approach toward understanding the histories of refractory materials within calcium-aluminum-rich inclusions (CAIs) in primitive meteorites. I apply high-spatial resolution techniques including electron backscatter diffraction (EBSD), transmission electron microscopy (TEM), and scanning transmission X-ray microscopy (STXM) enabled by focused ion beam scanning electron microscopy (FIB-SEM) to investigate CAI components and the Wark-Lovering Rims that surround them to obtain information on microstructure and crystal chemistry in meteorites with varied pre-terrestrial histories. These inclusions possess three-dimensional grain islands, which exhibit crystallographic preferred orientations. The islands formed by high-temperature condensation in the solar nebula in a process driven by surface energy minimization, as shown by density functional theory (DFT) calculations.

I also report preliminary results from laboratory experiments designed to synthesize perovskite under controlled temperature and oxygen fugacity ( $fO_2$ ) conditions. The goal of this project was to develop a calibrated barometer based on changes in the oxidation state of Ti and apply the barometer to measurements of meteoritic samples in order to infer the thermodynamic conditions under which meteoritic perovskite formed in CAIs.

# CHAPTER 1

## BACKGROUND

### 1.1 SCOPE OF THE THESIS

This thesis attempts to address problems related to the formation and evolution of CAIs such as (i) growth mechanics of Wark-Lovering Rims (WLRs); and (ii) the thermodynamic conditions in which refractory materials condensed or last equilibrated in the early solar nebula. The technical approach combines nanoscale analytical measurements with laboratory-based experiments to probe the fine-scale features of refractory inclusions. The thesis presents experimental data obtained on the petrography, chemistry, and crystal structure of CAIs and the WLRs that surround them and interprets the data in the context of the evolutionary history of these inclusions.

In Chapter 1, I provide an introduction to meteorites and their components, with an emphasis on CAIs. Chapter 2 describes the analytical techniques used in this work. Chapter 3 consists of a manuscript currently in preparation on the topic of oriented growth of WLRs for submission to the journal *Meteoritics and Planetary Science*. Chapter 4 presents some preliminary results on the development of a  $fO_2$  barometer, which is currently a work in progress and remains to be completed. The thesis concludes with a summary and an outlook of future work.

### 1.2 METEORITE CLASSIFICATION

Classification of meteorites is based on their mineralogical and petrographic characteristics as well as their O-isotopic compositions. A number of classification systems have been presented over the years, and much literature exists in field of meteorite taxonomy (McSween, 1977b; Wasson, 1985; Kallemeyn et al., 1996), to which the reader is referred for a comprehensive

review of the subject. For this thesis, I focused on petrologic type 3.0 chondrites. Chondritic meteorites, which derive from asteroids, are among the most primitive solar system materials (Wood, 1988). They are composed of a variety of components, including chondrules, calcium-aluminum-rich inclusions (CAIs), amoeboid olivine aggregates (AOAs), Fe, Ni-metal, and matrix. Chondrites are classified into groups, which in turn, are subdivided in classes: carbonaceous (CI, CM, CO, CV, CR, CH, CB, and CK), ordinary (H, L, and LL), and enstatite (EH and EL). Chondrites are also classified into petrologic types 1 through 6, reflecting the extent of thermal and aqueous processing (Van Schmus and Wood, 1967). Types 4 to 6 indicate increasing degrees of thermal metamorphism, while types 2 to 1 represent increasing degrees of aqueous alteration. Type 3.0 chondrites represent the most pristine, least altered materials, and so are ideal candidates for this study, which aims to probe the earliest nebular processes.

### **1.3 CALCIUM-ALUMINUM-RICH INCLUSIONS**

With radiometric age dates that exceed those of all other solar materials (Amelin et al., 2002), CAIs are widely accepted as being the first solids to have formed within our solar system. Analysis of them can provide a glimpse into some of the earliest chemical and physical processes to have transpired during solar system formation. CAIs are found in chondritic meteorites, mixed together with other heterogeneous materials. They are composed of mineral phases that form at very high temperatures and are predicted by thermodynamic models to be among the first solids to have condensed within a cooling gas of solar composition (Grossman, 1972; Ebel and Grossman, 2000; Lodders, 2003). CAIs, once thought to be pristine aggregates of high-temperature nebular condensates, are now universally recognized as having experienced prolonged histories of reactions with a nebular gas, reheating or multiple episodes of melting,

impact-induced shock, and secondary mineralization in the nebula or on asteroid parent bodies (Stoffler et al., 1991; Beckett et al., 2006; Fagan et al., 2007; Scott and Krot, 2005).

Many CAIs can be described as having a core-shell microstructure. The core of the generic CAI, as described by MacPherson (2004), consists of large (hundreds of  $\mu\text{m}$ ) melilite  $[(\text{Ca},\text{Na})_2(\text{Mg},\text{Fe},\text{Al},\text{Si})_3\text{O}_7]$  grains that surround smaller (tens of  $\mu\text{m}$ ) hibonite ( $\text{CaAl}_{12}\text{O}_{19}$ ) and spinel ( $\text{MgAl}_2\text{O}_4$ ) crystals intermixed with perovskite ( $\text{CaTiO}_3$ ). Surrounding many CAIs is a multilayered shell, measuring tens-of- $\mu\text{m}$  thick, which constitutes the WLR (Wark and Lovering, 1977). WLRs can also contain secondary phases such as anorthite ( $\text{CaAl}_2\text{Si}_2\text{O}_8$ ), calcic pyroxene ( $\text{CaMgSi}_2\text{O}_6$ - $\text{CaAl}_2\text{SiO}_6$ ), and forsterite ( $\text{Mg}_2\text{SiO}_4$ ). WLRs were hypothesized to have formed by several mechanisms including condensation, metasomatic exchange, and flash heating (Davis et al., 1986; Davis and MacPherson, 1994; Krot et al., 1995; Wark and Boynton, 2001).

Optical microscopy and electron microprobe studies have provided basic information on the properties of CAIs, which have contributed to our understanding of these objects as primary condensates (Grossman 1980; Armstrong et al. 1982; MacPherson and Grossman 1984). However, several reports note the presence of secondary phases that likely formed during parent-body processing or transport through the solar nebula (Cohen et al. 1983; Zolensky et al. 1993). Higher resolution techniques like transmission electron microscopy (TEM) have provided a glimpse into the fine-scale features of these inclusions. For example, hydration of CAI phases was examined by TEM and evidence for parent-body and nebular alteration was identified (Keller and Buseck, 1991; Greenwood et al., 1994). Greshake et al. (1998) examined the microstructure of CAIs in several CV chondrites with TEM and found evidence for condensation, shock processing, and slow cooling.

There is a large diversity of CAI types, and their populations and properties vary among meteorites. Fluffy type-A (FTA) and compact type-A (CTA) CAIs are distinguished on the basis

of differences in shape and texture. The latter tend to be more spheroidal in shape, have more magnesium-rich melilite exhibiting complex zoning, and hibonite tends to be concentrated around the CAI periphery in the vicinity of the WLRs (Simon et al., 1999). Trace element and petrologic evidence suggest that CTAs experienced partial melting (Beckett and Stolper, 1994). FTAs have highly irregular shapes and aggregate structures, aluminum-rich melilite that commonly is reversely zoned, and hibonite enclosed within the CAI interior (MacPherson and Grossman, 1984). These inclusions likely formed by condensation in the early solar nebula.

## CHAPTER 2

### ANALYTICAL TECHNIQUES

The information acquired from planetary materials can be maximized by performing coordinated analytical studies. I used a combination of non-destructive techniques like electron backscatter diffraction (EBSD) and electron microprobe to perform broad-scale surface analyses on CAIs. These measurements were combined with higher spatial resolution techniques including transmission electron microscopy (TEM) and scanning transmission X-ray microscopy (STXM) on CAI cross sections, enabled by focused-ion-beam scanning electron microscopy (FIB-SEM), to characterize fully their detailed crystal structure and chemistry. Below is a detailed description of these methods and how they were applied to address fundamental questions relating to the origin and evolution of CAIs.

#### 2.1 ELECTRON BACKSCATTER DIFFRACTION

EBSD is a surface characterization technique used in an SEM. It enables crystal orientation, phase distribution, and grain size to be determined on the surface of a material. EBSD patterns are generated on a phosphor screen by diffraction of electrons from a volume approximately 20 nm deep into the specimen. These diffraction patterns, known as Kikuchi patterns, are characteristic of the sample crystal structure and orientation.

The mechanism by which the diffraction patterns form is through inelastic scattering of the incoming electrons, some of which are incident on atomic planes at angles that satisfy Bragg's Law:

$$n\lambda=2d\sin\theta \quad (1)$$

where  $n$  is an integer,  $\lambda$  is the wavelength of the electron beam,  $d$  is the spacing of the lattice planes, and  $\theta$  is the angle of incidence. The electrons are diffracted to form a set of paired large

angle cones corresponding to each diffracting plane, which give rise to the characteristic Kikuchi bands of the electron backscatter diffraction pattern (Fig. 2.1).

An electron backscatter diffraction pattern consists of a large number of overlapping Kikuchi bands (Fig. 2.2). The nodes of these bands represent the intersection of zone axes in the crystal with the phosphor screen. The geometry of a Kikuchi pattern can be interpreted as a projection of the crystal lattice where the center of the projection represents the intersection of the primary beam with the specimen surface. Therefore, each Kikuchi band can be assigned the Miller indices of the diffracting crystal plane from which it originated. The width of the bands is related to the interplanar spacing according to the Bragg equation (1), and the angles between the bands correspond to the interplanar angles.

EBSD data acquisition was carried out on a Hitachi 3400N SEM equipped with an Oxford EBSD system located at the University of Arizona LaserChron Center. An accelerating voltage of 20 kV and an approximate incident beam current of 3.75 nA were used for all analyses. The stage was positioned at a 70° tilt from the horizontal. The Kikuchi patterns were indexed automatically in real time and the results were analyzed by the HKL Channel 5 software.

## **2.2 TRANSMISSION ELECTRON MICROSCOPY**

TEM was performed on cross-sections of CAIs to analyze their detailed crystal structure and chemistry. The TEM uses a high-energy (200 kV) electron beam transmitted through a very thin ( $\leq 100$  nm) sample to characterize the structure of materials. The electron column consists of an electron gun and a set of electromagnetic lenses operating in vacuum. Electrons are accelerated to energies in the range of tens to hundreds of keV, and they interact strongly with the sample to produce a wide range of signals represented schematically in Fig. 2.3. These include directly transmitted electrons, backscattered electrons, elastically and inelastically scattered electrons,

characteristic X-rays, and Auger electrons, all of which can be used to derive information on the complex nature of the specimen.

The most common mode of TEM operation is bright-field (BF) mode, where only the primary beam is utilized. In BF mode, an aperture is inserted in the back focal plane of the objective lens to allow only the transmitted beam to contribute to image formation (Fig. 2.4). The contrast of the transmitted wave is therefore dominated by amplitude rather than phase, so thick areas, or regions where heavy atoms are enriched, appear dark. Alternative contrast mechanisms, like Z-contrast imaging, can be implemented in scanning TEM (STEM) mode. By using a STEM detector with a large radius, a high-angle annular dark field (HAADF) image is formed by very high angle, incoherently scattered electrons. HAADF imaging is sensitive to variations in atomic number and so provides strong compositional sensitivity.

The TEM is also capable of producing diffraction patterns whereby highly localized structural and crystallographic information about crystalline materials can be obtained. The selected-area electron-diffraction (SAED) method uses parallel illumination of the sample and relies on the placement of an aperture in the image plane below the objective lens. If the sample is crystalline, the transmitted electrons scatter elastically off of the planes in the sample and produce spots in the SAED pattern. The spots, referred to as reflections, can be associated with a diffracting plane in the specimen according to Bragg's Law (1). SAED patterns can be indexed to determine the structure and orientation of the diffracting crystal based on calibrated camera constants unique to the microscope.

Specimen thickness is a crucial issue in TEM analysis. The sample must be thin enough for the beam to be transmitted and for proper scattering to occur. High quality samples will have a thickness that is comparable to the mean free path of the electrons, but in general, TEM specimens should be less than 100 nm thick. However, higher accelerating voltages can tolerate

thicker specimens. To achieve the desired thickness, the sample must be modified and this is discussed below in §2.3.

The work presented herein used a 200 keV JEOL 2010F TEM equipped with an EDAX energy-dispersive X-ray spectrometer (EDS) at Arizona State University and a 200 keV JEOL 2500SE TEM equipped with a ThermoNoran EDS and STEM detectors at NASA Johnson Space Center.

### **2.3 FOCUSED-ION-BEAM SCANNING X-RAY MICROSCOPY**

TEM analysis of bulk samples requires modifying their geometry to fit within the sample holder (3 mm diameter) and milling them to electron transparency. The focused ion beam has been successfully used as a means to prepare site-specific thin sections from bulk material for subsequent analysis by TEM. This tool was originally developed for the semiconductor industry to look at nanoscale defects in electronic devices, but it has since been applied to a range of earth and planetary materials including presolar grains, primitive meteorites, and terrestrial minerals (Stroud et al., 2004; Zega et al., 2010; Busemann et al., 2009; Floss et al., 2014; Nguyen et al., 2010). The development of a combination FIB and scanning electron microscope (FIB-SEM) combines the imaging and analytical capabilities of an SEM with the etching capabilities of an ion beam (Giannuzzi and Stevie, 2005). With FIB-SEM, radiation-hard materials, such as those that occur within CAIs and WLRs, can be site-specifically extracted and ion-milled to electron transparency.

Creating an electron-transparent section begins with the deposition of a thin carbon strap over the region of interest (Fig. 2.5). This serves to protect the underlying sample from ion implantation and radiation damage. Material is then removed from either side of the carbon strap using a focused beam of  $\text{Ga}^+$  ions. The section is extracted with a tungsten needle, welded to a

TEM support grid (typically composed of Cu or Mo), and thinned in situ to less than 100 nm in thickness using a beam of Ga<sup>+</sup> ions to iteratively shave away material from either side. The end result is an electron transparent wafer suitable for TEM analysis. For this study, samples were prepared with an FEI Nova 200 FIB-SEM at Arizona State University and an FEI Quanta 3D FIB-SEM at NASA Johnson Space Center.

## 2.4 SCANNING TRANSMISSION ELECTRON MICROSCOPY

X-ray near-edge structure (XANES) spectroscopy was performed using the Scanning transmission X-ray microscope (STXM) on beamline 5.3.2 at the Advanced Light Source (ALS), Lawrence Berkeley National Laboratory. The synchrotron light source produces high-brightness, monochromatic X-rays, which are directed through a bending magnet and focused using a zone plate lens to approximately 35 nm in diameter with energy resolution of better than 100 meV (Kilcoyne et al., 2003). High spectral resolution is needed to reveal the near-edge structure and chemical shift that is fundamental to measuring changes in oxidation state. Spectra were acquired in one-dimensional line-scan mode or as two-dimensional image stacks, where the average X-ray absorption was averaged over a selected region of pixels in a series of aligned images (Jacobsen et al., 2000). The energy shift between subsequent X-ray images could be controlled by a spherical grating monochromator and was selected to be 0.1 eV in the region of the Ti L<sub>2,3</sub> absorption edge between 454 eV and 470 eV with a dwell time of 6 ms. XANES data analysis was performed using the custom software suite aXis2000 (Hitchcock et al., <http://unicorn.mcmaster.ca/aXis2000.html>).

XANES spectroscopy is a sensitive tool that probes unoccupied electronic states above the Fermi level (Fig. 2.6). The fundamental phenomenon underlying XANES is the absorption of an X-ray photon followed by promotion of a core electron to an excited state. When the incident X-

ray has an energy equal to that of the binding energy of the core electron, there is a sharp rise in absorption, known as an absorption edge. The Ti L-edge XANES spectra show several well-resolved features due to excitations of  $2p$  core electrons into empty  $3d$  states. As a result of spin-orbit coupling in the  $2p$  state, the spectra display two prominent features in the energy ranges 455 to 461 eV and 461.2 to 468 eV, corresponding to the  $L_3$  ( $2p_{3/2} \rightarrow 3d$ ) and  $L_2$  ( $2p_{1/2} \rightarrow 3d$ ) absorptions, respectively. The multiple structures are due to the strong Coulombic interaction between poorly screened  $3d$  electrons and the  $2p$  core hole. The  $L_2$  edge features are broadened relative to the  $L_3$  edge because of a shorter lifetime of the  $2p_{1/2}$  core hole (i.e., a radiationless electron transition from  $2p_{3/2}$  to  $2p_{1/2}$ ), accompanied by the promotion of a valence electron into the conduction band. Under the  $O_h$  crystal field, the  $3d$  band splits into  $t_{2g}$  (formed by  $d_{xy}$ ,  $d_{xz}$ , and  $d_{yz}$  orbitals) and  $e_g$  (formed by  $d_x^2 - y^2$  and  $d_z^2$ ) sub-bands.

## 2.5 ELECTRON MICROPROBE

I used a Cameca SX-100 electron microprobe at the Lunar and Planetary Laboratory, University of Arizona for obtaining images and representative mineral compositions of CAI thin sections. The electron microprobe is an SEM equipped with wavelength- and energy-dispersive X-ray spectrometers. It is an analytical tool used to image materials and for quantitative analysis of their chemical composition. Like other electron microscopes, an electron microprobe has an electron column, at the top of which is an electron gun. Electrons are accelerated (5-30 keV) from the gun by an electrical potential. As the electrons travel down the column, they are focused by a pair of electromagnetic lenses. The volume of material excited by the electron beam typically ranges from 1 to 5  $\mu\text{m}$  in depth. Consequently, highly localized compositional information can be obtained.

Characteristic X-rays are the main signal used in electron microprobe analysis, and are observed at energies corresponding to the allowed electronic transitions of the elements in the sample. The incident beam causes an inner shell electron to be ejected from an atom, leaving behind a hole. An electron from an outer shell fills the hole, and the difference in energy results in the emission of an X-ray photon. For quantitative analysis, it is necessary to select and measure the X-rays produced by a specific element. In wavelength dispersive spectrometry (WDS), this is done using X-ray spectrometers. A high-resolution diffracting crystal separates the X-ray line of interest from other characteristic X-rays emitted by the sample. The necessary condition for constructive diffraction of X-rays by a crystal is described by Bragg's Law (1).

The fundamental assumption in electron microprobe analysis is that the intensity of an X-ray is directly proportional to the concentration of the emitting element in the sample. This relationship is embodied in Castaing's approximation:

$$\frac{C_{\text{unk}}^A}{C_{\text{std}}^A} = \frac{I_{\text{unk}}^A}{I_{\text{std}}^A} \quad (2)$$

where  $C_{\text{unk}}^A$  is the concentration of species A in the unknown,  $C_{\text{std}}^A$  is the concentration of species A in the standard,  $I_{\text{unk}}^A$  is the X-ray intensity in the unknown, and  $I_{\text{std}}^A$  is the X-ray intensity in the standard (Goldstein et al., 1992). This simple ratio does not hold in practice because matrix effects need to be considered in order to obtain accurate quantitative results. In the ZAF matrix correction scheme, correction factors for atomic number (Z), absorption (A), and secondary fluorescence (F) are applied to Castaing's approximation (2). The atomic number correction adjusts for the loss in X-ray intensity due to inelastic scattering in the material. The absorption correction accounts for the loss in X-ray intensity due to absorption in the material. The fluorescence correction accounts for the creation of secondary X-rays resulting from fluorescence in the sample.

## 2.6 ENERGY DISPERSIVE X-RAY SPECTROSCOPY

Energy dispersive X-ray spectroscopy (EDS) is an analytical technique employed in electron microscopes. Like WDS, EDS relies on the detection of characteristic X-rays to identify the elements present in a material. However, in contrast to WDS, X-rays from the sample deposit their energy in a semiconductor detector, where electrons are transferred from the valence band to the conduction band, thereby creating electron-hole pairs. Electrons and holes are separated by a reverse bias to form a charge pulse, which is then converted to a voltage pulse. An EDS spectrum is constructed by measuring the energy of the emitted X-rays and counting the number of signals for a specific energy. After a sufficient number of counts, the peaks for a specific element can be easily identified.

For quantitative EDS analysis, the wt.% of each element can be related to the measured X-ray intensities according to the Cliff-Lorimer equation:

$$\frac{C_A}{C_B} = k_{AB} \frac{I_A}{I_B} \quad (3)$$

where  $C_A$  is the concentration of element A,  $C_B$  is the concentration of element B,  $I_A$  is the X-ray intensity of element A,  $I_B$  is the X-ray intensity of element B, and  $k_{AB}$  is a correction factor, which depends on the particular TEM/EDS system. If the specimen is thin enough to assume no absorption and no fluorescence, then  $k_{AB}$  only depends on the atomic number.

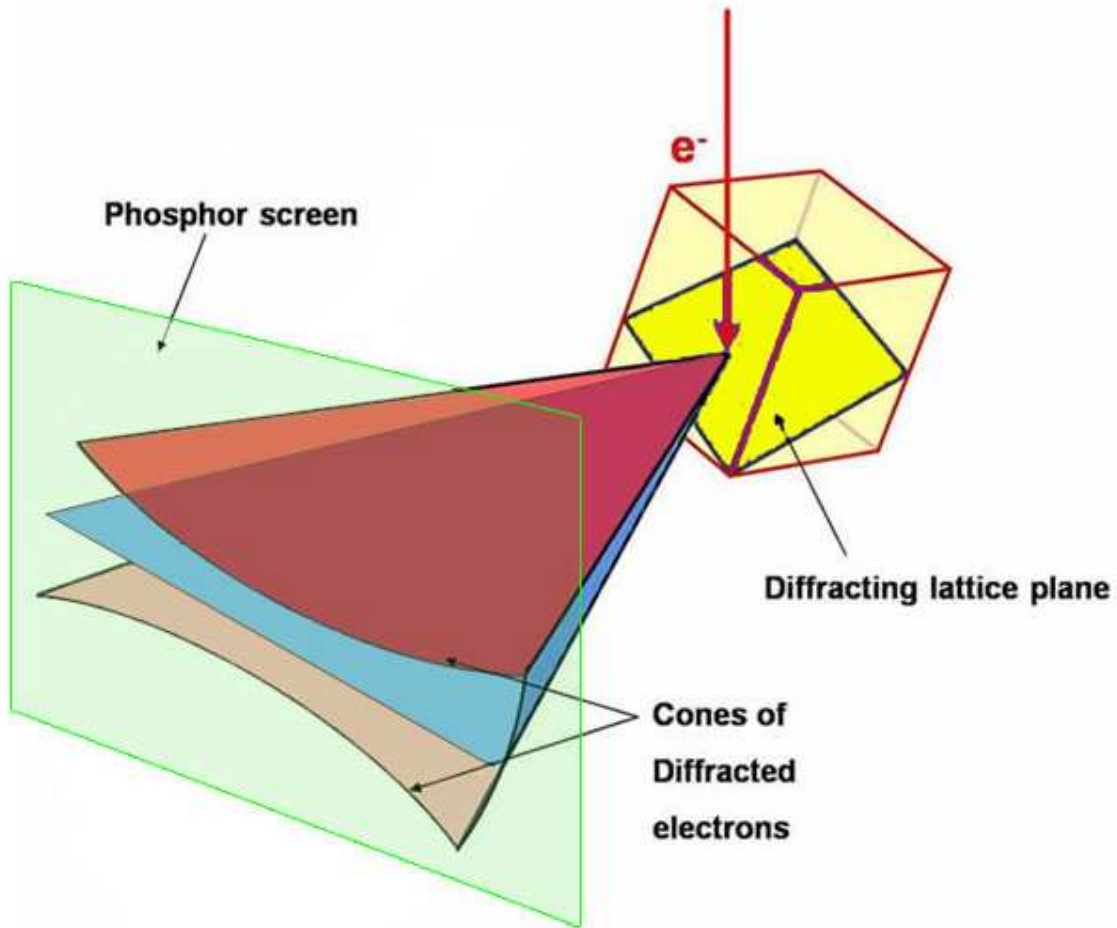


Fig. 2.1 Formation of the electron backscattered diffraction pattern. Electrons incident on crystal planes at the Bragg angle are diffracted into a pair of cones to form Kikuchi bands in the diffraction pattern. From <http://www.ebsd.com>.

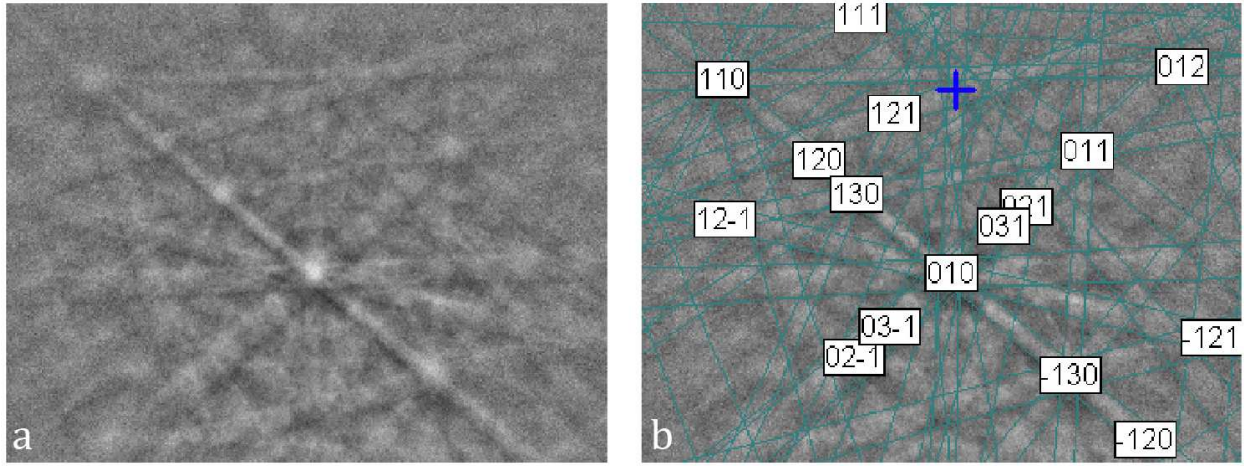


Fig. 2.2 (a) A Kikuchi diffraction pattern of diopside. (b) The same pattern indexed and labelled with the Miller indices of each diffracting plane.

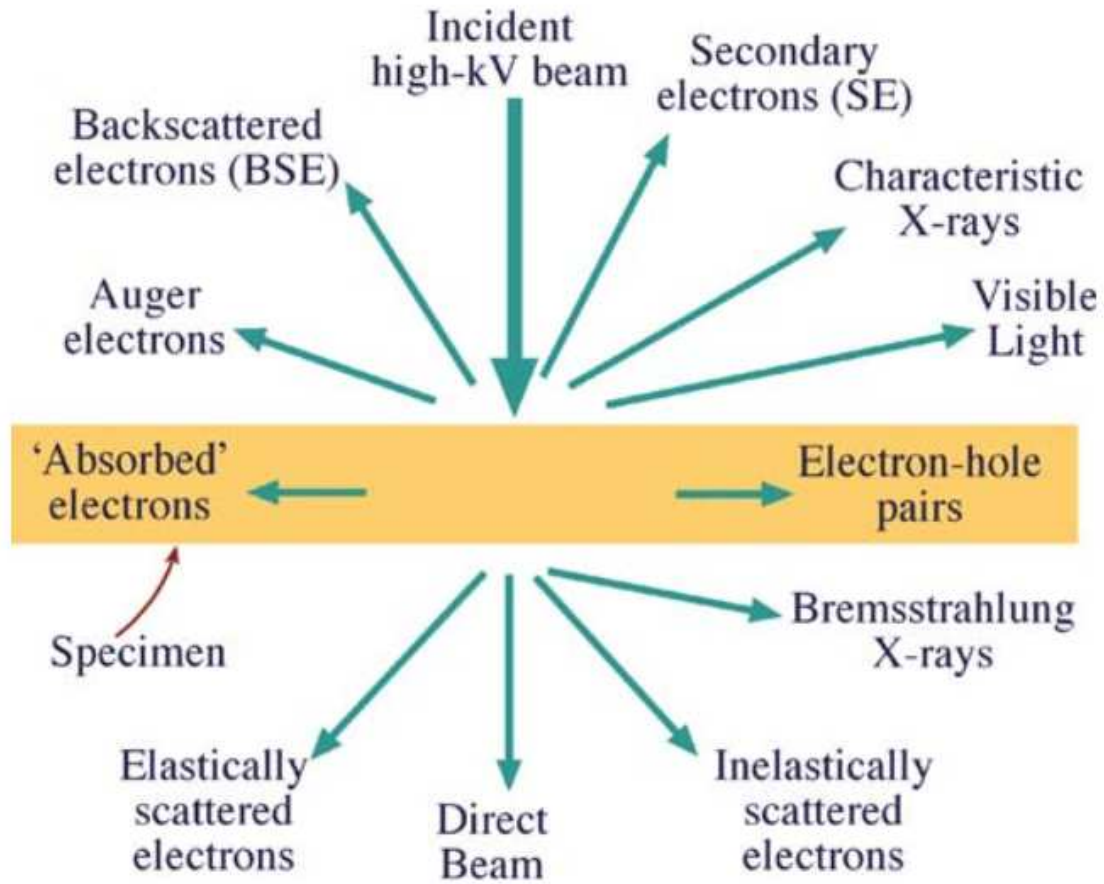


Fig. 2.3 Signals generated when a high-energy beam of electrons interacts with a thin specimen. From *Transmission Electron Microscopy* by Williams and Carter.

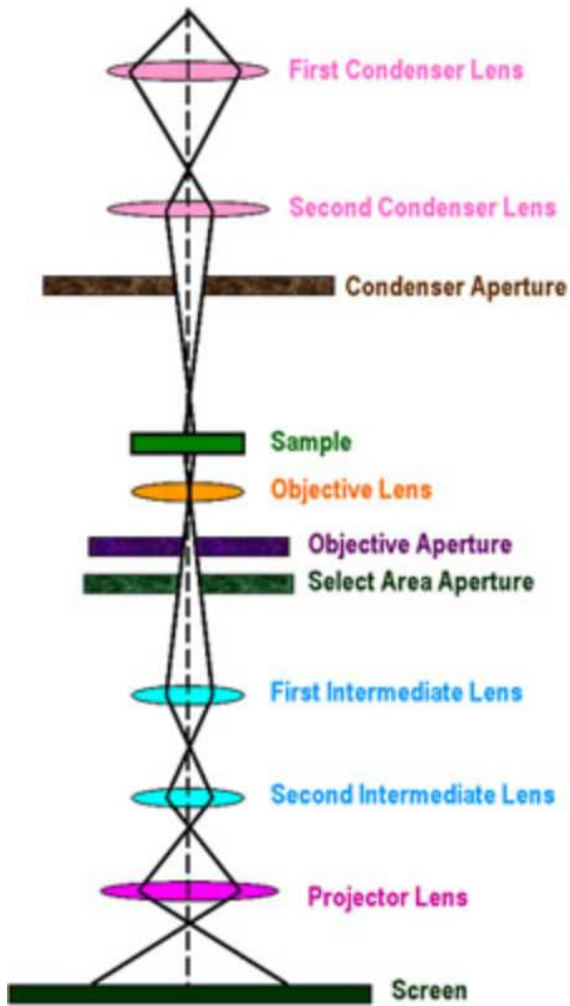


Fig. 2.4 Optical diagram of a TEM. Illumination from a source is focused by the condenser lens onto the specimen. A first magnified image is formed by the objective lens. This image is further magnified by the projector lens onto a fluorescent screen. Modified from *Transmission Electron Microscopy* by Williams and Carter.

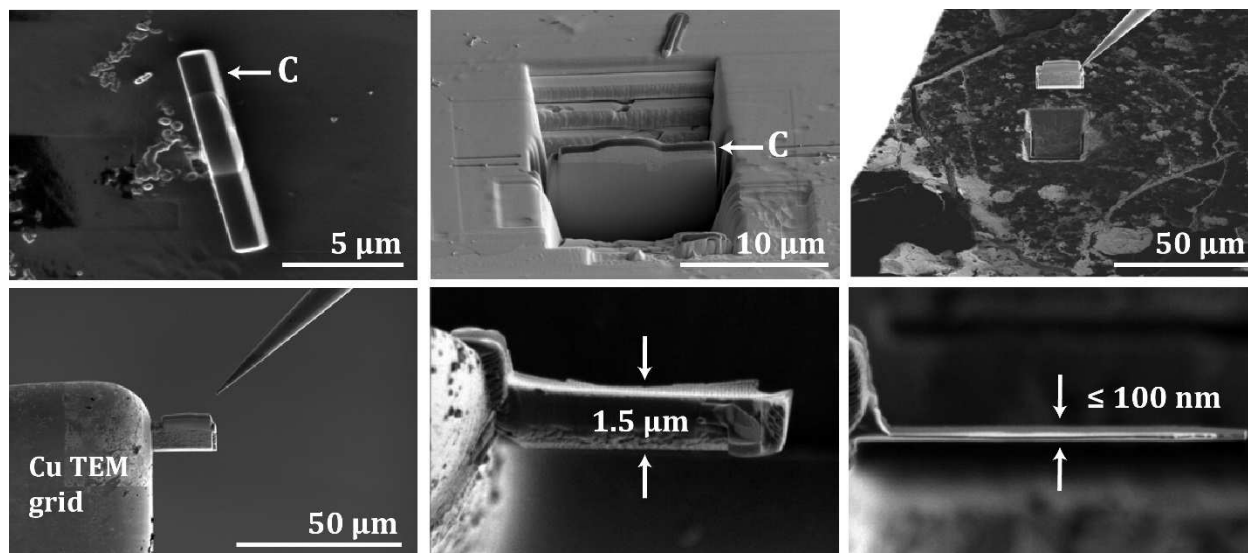


Fig. 2.5 Procedure for extracting an electron transparent section using the FIB-SEM. Images acquired by Professor Zega (unpublished data).

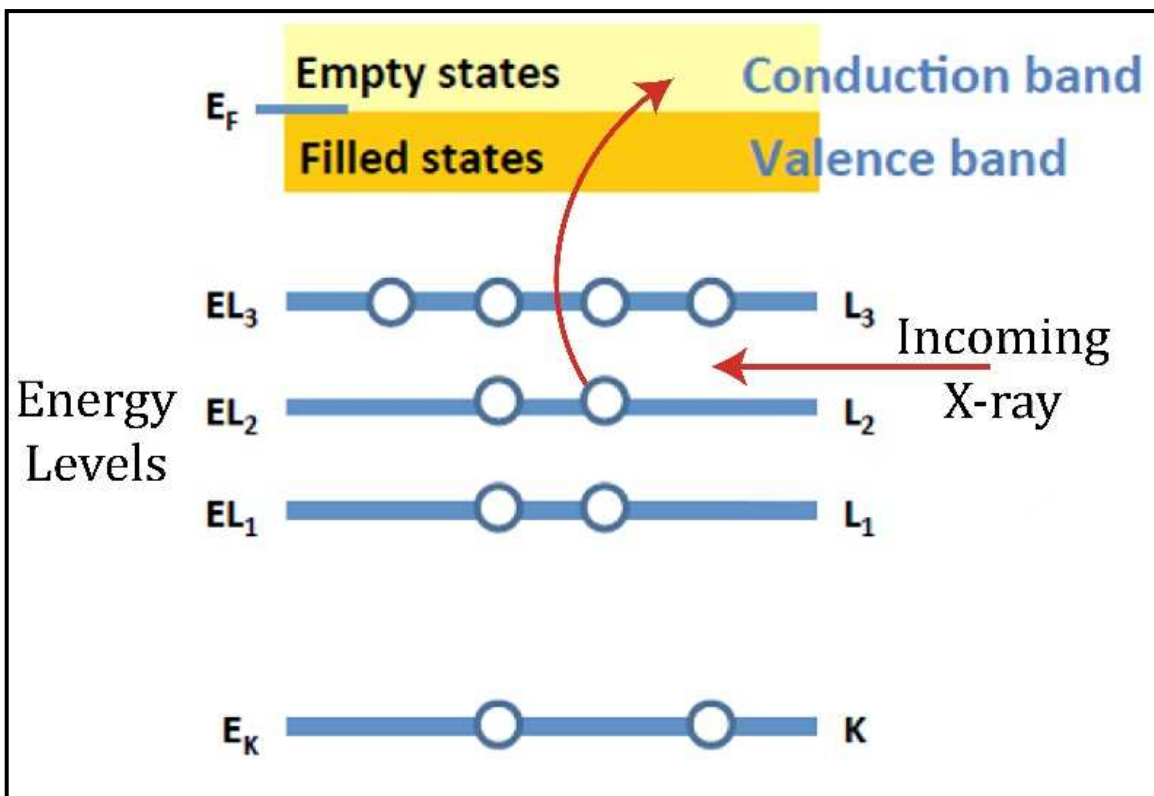


Fig. 2.6 Schematic illustration of X-ray absorption in a transition metal atom. In the figure, electron transitions can occur from the K and L core shells. Modified from *Transmission Electron Microscopy* by Williams and Carter.

## CHAPTER 3

### MICROSTRUCTURAL ANALYSIS OF WARK-LOVERING RIMS

#### 3.1 INTRODUCTION

CAIs are mm- to cm-sized inclusions that occur in chondritic meteorites and are composed of refractory mineral phases that form at very high temperatures. These phases are predicted by thermodynamic models to be among the first solids to have condensed from a cooling gas of solar composition (Grossman, 1972; Ebel and Grossman, 2000; Lodders, 2003; Ebel, 2006), and so they can provide insights into the chemistry of the early solar system. Surrounding many CAIs is a multilayered shell called a WLR (Wark and Lovering, 1977). WLRs were hypothesized to have formed by several mechanisms including condensation, metasomatic exchange, and flash heating (Grossman, 1975; Davis et al., 1986; Davis and MacPherson, 1994; Krot et al., 1995; Wark and Boynton, 2001; MacPherson, 2004).

CAI types include irregularly shaped fluffy type A (FTA) inclusions and rounded compact type A (CTA) inclusions. MacPherson and Grossman (1984) described FTAs as containing Al-rich melilite, V-rich spinel, perovskite, and hibonite that likely formed by condensation in the early solar nebula. The CTA inclusions were recognized by MacPherson and Grossman (1979) as having spheroidal shapes and zoned Mg-rich melilite. It is generally believed that most CTAs crystallized from melts (Simon et al., 1999) based on dynamic crystallization experiments on synthetic analogs (Beckett et al., 2006).

The optical microscope and electron and ion microprobes have been used extensively to tease out information on the properties of CAIs and have provided a wealth of information on their origins (Armstrong et al., 1982; MacPherson et al., 1983; Ireland, 1988; Kornacki and Wood, 1984; Simon et al., 1994; Krot et al., 1995). In comparison, there are fewer studies that have

investigated the crystal chemistry and structure of CAIs, but these have provided valuable glimpses into their complex microstructures (Doukhan et al., 1991; Greshake et al., 1998; Keller and Buseck, 1991; Barber et al., 1984). The advent of FIB-enabled TEM studies provided a new way of gaining insights into site-specific features of meteorites (Heaney et al., 2001; Lee et al., 2003; Stroud et al., 2000) including CAIs. Here we build on earlier efforts aimed at understanding the detailed microstructural features of CAIs (Toppani et al., 2006; Zega et al., 2007, 2009, 2010; Paque et al., 2009, Ma et al., 2011). We apply EBSD and TEM enabled by FIB-SEM to the analysis of WLRs in a CTA and a FTA from meteorites with varied preterrestrial histories. There are a number of important parameters that are now routinely available from EBSD analysis but that are not obtainable from conventional methods of microstructural characterization. These include local relationships between microstructure and orientation as well as information on grain and phase boundaries. Combined with TEM, our goal is to obtain coordinated three-dimensional crystallographic information about WLRs in order to gain new insights into their formation and evolution.

### **3.2 SAMPLES AND METHODOLOGY**

I investigated a CTA previously identified in a thin section of Axtell (AX30, Smithsonian) and an FTA identified in a thin section of Allende (TS25, U. Chicago). Axtell and Allende are both part of the oxidized sub-group of CV3 chondrites. These samples were chosen in order to compare the crystallographic features of previously molten refractory inclusions (CTAs) to those that are believed to have condensed from the nebular gas (FTAs). I used a Cameca SX-100 electron microprobe to obtain backscattered electron (BSE) images of the entire thin sections (Fig. 3.1). These images were stitched together to form mosaics of the entire thin section and select specific sites for detailed analysis using EBSD and TEM.

In order to achieve a surface quality appropriate for EBSD measurement, the surfaces of the thin sections were polished using 1  $\mu\text{m}$  diamond paste followed by 0.05  $\mu\text{m}$  colloidal silica on an automatic VibroMet 2 Vibratory Polisher for a minimum of three hours. After polishing, samples were coated with a thin layer of carbon to avoid surface charging. EBSD data acquisition was carried out on a Hitachi 3400N SEM equipped with an Oxford EDS/EBSD system. An accelerating voltage of 20 kV and an approximate incident beam current of 3.75 nA were used. The stage was positioned at a 70° tilt from the horizontal. The Kikuchi diffraction patterns were indexed automatically in real time and the results were analyzed using HKL Channel 5 software. Pattern-quality and Euler-orientation maps were constructed with a 500 nm step size and a dwell time of 0.5 seconds. For each CAI, areas of roughly 100 $\times$ 100  $\mu\text{m}$  were analyzed containing several thousand individual grains ranging in size from 0.5 to tens of microns in diameter. Data were corrected by extrapolating zero solutions with seven neighbors followed by elimination of wild spikes. To ensure that there was no bias toward larger grains, the data set was further reduced to one point per grain. Once the data were processed, each point, representing a single grain, was plotted on an equal-area upper-hemisphere pole-figure plot with data clustering of 5° and a half-width of 10°.

Following broad-scale EBSD measurements, I selected specific sites for detailed analysis using TEM. Sites were chosen based on where EBSD revealed the presence of a preferred crystallographic orientation on the surface. The regions were extracted and thinned to electron transparency with an FEI Nova 200 FIB-SEM at Arizona State University and an FEI Quanta 3D FIB-SEM at NASA Johnson Space Center. The FIB sections were analyzed with a 200 keV JEOL 2010F TEM equipped with an EDAX energy-dispersive X-ray spectrometer (EDS) located at Arizona State University and a 200 keV JEOL 2500SE TEM at NASA JSC equipped with a ThermoNoran EDS and both STEM-based BF and DF detectors. Mineral structure was

determined using selected-area electron-diffraction (SAED). All SAED patterns were measured with the crystallographic image processing software package (CRISP) based on calibrated camera constants and indexed to the appropriate reference structures.

Density functional theory (DFT) calculations were performed in order to model the atomic structures of the WLR layers. Calculations were performed using the Vienna Ab-initio Simulation Package (VASP) version 5.2 (Kresse and Furthmüller, 1996; Kresse and Joubert, 1999). DFT calculations were performed assuming a periodically repeated simulation super cell and a vacuum space of 15 Å to prevent spurious interactions between the periodic surfaces. A convergence criterion that ensures all atomic forces are smaller than 0.02 eV/Å was imposed while locating energy-minimized surfaces.

### **3.3 RESULTS**

#### **3.3.1 PETROGRAPHY AND MINERALOGY**

Axtell AX30 is a CTA that consists primarily of melilite with minor perovskite and spinel (Fig. 3.1). Microprobe analysis revealed that most of the melilite is relatively Mg-rich ( $Ak_{22-28}$ ). However, melilite nearer the interior of the inclusion is slightly more gehlenitic ( $Ak_{17-19}$ ). A WLR sequence (40-50 μm) surrounds the entire inclusion and consists of an outermost continuous layer of pyroxene overlying a layer of spinel intergrown with perovskite. There is Mg-Al spinel with minor Ti (0.5 wt.%). Perovskite grains contain minor V (0.2 wt.%). Pyroxene is Mg- and Ca-rich with decreasing  $TiO_2$  content outward from the inclusion.

Allende TS25 is a FTA that consists of large, reversely zoned melilite ( $Ak_{20-10}$ ) crystals with inclusions of spinel, hibonite, and perovskite (Fig. 3.2). This inclusion was described in detail by MacPherson and Grossman (1984) and Cosarinsky et al. (2008). The WLR sequence (20-30 μm)

consists of three distinct layers of stoichiometric spinel, anorthite, and Ti-rich pyroxene grading outward from the inclusion.

### 3.3.2 EBSD ANALYSIS

Crystal orientation and microstructure of pyroxene surface grains within the WLRs were investigated by EBSD. I focused on pyroxene because it was previously reported that oriented pyroxene grains were found in the WLRs of Allende and Vigarano (Zega et al., 2009, 2010). Grain orientations are given in terms of Euler angles, which relate the orientation of individual grains to the sample coordinate system. For orientation maps, false colors are generated by the superposition of three color channels (red, green, and blue), which are correlated to the values of the three Euler angles ( $\varphi_1$ ,  $\Phi$ ,  $\varphi_2$ ) of each measured pixel. Therefore, similar colors represent similar grain orientations.

The crystallographic orientations are displayed as pole figures, which map a selected set of crystal plane normals plotted with respect to the specimen reference frame. Thus, an  $\{hkl\}$  pole figure shows the distribution of the  $hkl$  poles in the sample. The crosshairs of the pole figure represents the surface normal of the specimen. Pole figures express the probability of finding a lattice plane in a certain sample direction in multiples of uniform density (m.u.d.). A m.u.d. of one indicates randomly oriented grains; a m.u.d. greater than one is indicative of a preferred orientation.

In AX30, I measured a total of 3,023 grains within the WLR. These grains have equivalent diameters ranging from 0.5 to 17  $\mu\text{m}$  with the majority under 5  $\mu\text{m}$  and only four grains over 10  $\mu\text{m}$ . Of those 3,023 grains, 1,358 are pyroxene. The remaining grains include spinel, perovskite, and melilite. An extensive portion (~42% or 575 grains) of this region of the pyroxene layer possesses similarly oriented augite grains (Fig. 3.3a). These are represented on upper-hemisphere equal-area projections (Fig. 3.3b). Each pole figure has a single hot spot, indicating that this

subset of augite grains is dominated by a single orientation. The distance of the hot spot relative to the crosshairs reflects the angular variation of the grains from the specimen normal direction. The {100} poles are oriented within  $52^\circ$  of surface normal; the {010} poles are oriented within  $43^\circ$ ; and the {001} poles are oriented within  $45^\circ$ .

In TS25, I measured a total of 8,082 grains within the WLR. These grains have equivalent diameters ranging from 0.5 to 12  $\mu\text{m}$  with the majority under 3  $\mu\text{m}$  and only two grains over 10  $\mu\text{m}$ . Of those 8,082 grains, 1,569 are pyroxene. The remaining grains include spinel, hibonite, perovskite and melilite. A portion (~38% or 603 grains) of the pyroxene layer possesses similarly oriented diopside grains (Fig. 3.4a). The crystal orientations of the diopside grains are shown on the upper-hemisphere equal-area projections (Fig. 3.4b). For diopside, the density of {100} poles is distributed between two hotspots located at polar angles of  $33^\circ$  and  $83^\circ$ . The {010} poles are also distributed between two hotspots at  $75^\circ$  and  $36^\circ$ . The {001} poles are oriented within  $62^\circ$  of surface normal.

EBSD also shows that clusters of anorthite grains within the WLR have similar orientations (Fig. 3.4c). Of the 8,082 total grains, 112 are anorthite. Each pole figure has a single hot spot, indicating that this subset of anorthite grains is dominated by a single orientation. The anorthite {100} poles are oriented  $87^\circ$  from normal, nearly parallel to the surface of the thin section. The {010} poles are oriented within  $67^\circ$ ; and the {001} poles are oriented with  $60^\circ$ .

### **3.3.3 TEM CROSS-SECTIONAL ANALYSIS**

A TEM study of the WLRs in TS25 and AX30 was performed in order to characterize subsurface relationships and compare them with surface trends. FIB sections were extracted from areas where EBSD revealed the presence of similar crystallographic orientations (see Figs. 3.1 & 3.2 for locations of transects). The FIB section of AX30 transects and consists entirely of

pyroxene (Fig. 5a). I acquired EDS spectrum images and SAED patterns to verify the pyroxene composition and structure. Standardless quantification of EDS spectra from part of the pyroxene gives a composition of  $(\text{Ca}_{1.0}\text{Mg}_{0.8}\text{Ti}_{0.1})(\text{Si}_{1.7}\text{Al}_{0.4})\text{O}_6$  (Fig. 3.5b). Measurements of interplanar spacing and angles from SAED patterns are consistent with orthopyroxene. I acquired SAED patterns from multiple grains and found a consistent [120] orientation among them (Fig. 3.5c-d).

In comparison, the FIB section of TS25 transects anorthite, Ti-rich pyroxene, spinel, and perovskite as revealed by EDS maps (Fig. 3.6a-b). Standardless quantification of EDS spectra is consistent with a nominally stoichiometric anorthite  $\text{Ca}_{1.0}\text{Al}_{2.1}\text{Si}_{1.9}\text{O}_8$  composition. Spinel is  $\text{MgAl}_2\text{O}_4$  with low concentrations (<0.5 wt.%) of Ti and Fe (Fig. 3.6b). Ti-rich pyroxene has a composition of  $(\text{Ca}_{1.0},\text{Mg}_{0.6},\text{Ti}_{0.3})(\text{Si}_{1.5},\text{Al}_{0.5})\text{O}_6$ , consistent with diopside (Fig. 3.6c). Measurements of interplanar spacing and angles from SAED patterns acquired from multiple grains are consistent with anorthite [010] and diopside [13-4] (Fig. 3.6d-f). SAED patterns acquired from several areas show no angular variation among the diopside crystals.

### 3.3.4 DENSITY FUNCTIONAL THEORY SIMULATIONS

DFT simulations were used to gain further insight into the structure of the interface between diopside and anorthite layers in the WLR of TS25. In order to construct a model of the interface, we generated diopside (13-4) and anorthite (010) surfaces from their respective crystalline phases based on the orientations of the crystals revealed by TEM. The interface was built by placing one surface on top of the other, and the structures were relaxed to their local energy minima. We note there is limited commensuration between the diopside and anorthite lattices, and as a consequence, the mismatch between the surfaces requires using the average of the lattice vectors of the two surfaces to generate the interface.

A thermodynamically stable interfacial structure was formed between diopside and anorthite only if the respective lattices were strained by 1.15-1.17% and 3.26-3.49% in the *a* and *b* directions. Based on the following equation

$$\Delta E = E_{\text{Int}} - E_{\text{An}} - E_{\text{Di}} \quad (4)$$

where  $E_{\text{Int}}$ ,  $E_{\text{An}}$  and  $E_{\text{Di}}$  is the total energy of interface structure, anorthite and diopside surfaces, respectively, the interfacial energy was found to equal 5.39 eV for standard surfaces and -6.34 eV for strained surfaces. The fact that the respective lattices have to accommodate strain to enable an energetically stable interface implies either thermal or impact processes were active during interface formation.

The interface is characterized by ionic bonds formed between the electropositive and electronegative surface atoms of anorthite and diopside, respectively. Specifically, for diopside (13-4), the surface atoms are O, Ca, and Mg, whereas for anorthite (010), the surface atoms are O and Mg. While the anorthite and diopside lattices are strained parallel to the interface, there is no noticeable structural reconstruction in the lateral direction.

### 3.4 DISCUSSION

The obtained Euler maps show a distribution of orientations within each of the CAIs. There are clusters of grains within individual WLR layers that share common orientations and there are similar orientations between the WLR layers. These results suggest that the variety of crystal orientations are due to a combination of structural energetics and growth kinetics.

For TS25, the EBSD data reveal a preferred orientation among diopside grains within the WLR. The hot spot in the {001} pole figure (Fig. 3.4b) indicates that the highest concentration of c-axes cluster around a single hotspot, which is elevated about 30° from the surface of the thin section. There is also a preferred internal orientation among anorthite grains within the WLR.

The hot spot near the bottom of the {100} pole figure indicates that the highest concentration of a-axes is aligned nearly parallel to the surface of the thin section.

TEM analysis of the FIB section from TS25 revealed that diopside crystals below the surface also cluster in similar orientations to one another, which corroborates the trend observed on the surface with EBSD. These diopside grains index to [13-4] and are adjacent to a large anorthite [010] grain (Fig. 3.6d-f). It should be noted that the orientations at depth are not necessarily identical to those on the surface because the view in cross section is shifted 90° from the surface. Nonetheless, the same trend of clusters of similarly oriented grains is observed in cross section, which indicates that the same process that led to oriented grains extending across the surface of the CAI was active in three dimensions and led to the formation of clusters of grains at depth. The DFT calculations show that the formation of a thermodynamically favorable interface is due to the structural properties of the individual WLR layers.

The endothermic nature of interface formation between the diopside and anorthite standard surfaces can be understood based on the fact that there is a substantial angle mismatch (~10°) between them. When substantial mismatch between two heterostructures occurs, a coherent interface is highly unlikely to form. In the context of CAI and WLR rim growth, this result suggests that mechanical attachment, i.e., previously formed grains accreting to the surface, rather than chemical bonding would be expected. However, it is clear from the morphology of the WLR layers that a coherent interface occurs around TS25 (Fig. 3.6a). In comparison, when strained surfaces are used, the energy is thermodynamically favorable to interface formation. Given the high-temperatures expected for condensation of WLR phases (e.g. 1450K for diopside and 1326K for anorthite; Grossman, 1972), it is plausible that such conditions could have led to a shift in the lattice parameters of diopside and anorthite. The resulting strained surfaces likely led

to the coherent interface observed here and therefore favors a condensation origin for at least part of the WLR observed here for TS25.

Based on the similar positions of hot spots in the diopside and anorthite pole figures, an orientational relationship must exist between these two phases in TS25. I hypothesize that grain nucleation begins with pre-existing grain boundaries, which serve as seed nuclei, along directions controlled primarily by the structure of the melilite inclusion or the most internal WLR layer. These surfaces act as nucleation sites on which the WLR can condense from the surrounding nebular gas and dust (Fig. 3.7a). As growth proceeds, clusters of anorthite and diopside grains condense with similar orientations, producing island-type growth. Ultimately, the islands will merge together creating the observed microstructure (Fig. 3.7c). Coalescence of the grain clusters is likely controlled by a mechanism that favors aggregation of similarly oriented grains and destroys strongly misoriented ones. The DFT calculations suggests that this process is driven by minimization of surface free energy. Specifically, the local condensing system can reduce its free energy by forming an interface from the strained surfaces as indicated by the calculated interface energy of -6.34 eV, which is energetically favorable.

The materials-science community has long relied on island-growth models to describe atomistic processes that occur during vapor-phase thin film growth. For example, Parker et al. (1999) described the vapor deposition of gold onto (110) planes of  $\text{TiO}_2$  where coverage of Au islands increased with the defect density of the  $\text{TiO}_2$  substrate. Also, Maranville et al. (2006) described the vapor deposition of  $\text{CoPt}_3$  films in which nucleation and growth occurred mostly on step edges. In the case of CAIs, the growth of islands would depend on the nature of the surface, e.g., defects and step edges, as well as the fraction of the atoms arriving at the surface of the CAI from the surrounding gas and dust. Given the irregularity of the melilite surface around fluffy type-A CAIs like that observed here in TS25, it seems likely that some amount of defects

and step edges would occur and serve as nucleation sites for the first WLR layer. Supporting evidence for such surface irregularities is provided by Muller and Wlotzka (1982), who reported melilite with high dislocation densities as well as point defects in anorthite in the Leoville CV3 chondrite. Further, Barber et al. (1984) reported high dislocation densities and considerable internal strain in melilite crystals in an FTA CAI from Allende. These studies show that the CAIs possess defect structures that could mediate the subsequent nucleation of WLR phases.

In hetero-epitaxial growth, there is mismatch between the lattice constants for the substrate and the deposited film (Hwang and Bartelt, 1997; Shchukin and Bimberg, 1999). For large lattice mismatch, as is the case between diopside and anorthite, local structural disorder and excess energy lead to a prevalence of three-dimensional rather than two-dimensional islands (Evans et al., 2006), which correlates well with our experimental observations. EBSD revealed clusters of oriented grains extending over the surface of the thin section and TEM showed clusters of oriented grains below the surface, for both AX30 and TS25.

For AX30, the EBSD data reveal a preferred orientation among augite grains within the WLR. All the grains have approximately the same orientation and therefore cluster around a single hot spot. All three principal directions ( $\{100\}$ ,  $\{010\}$ , and  $\{001\}$ ) show clustering (Fig. 3.3b), suggesting that the measured grains nucleated together in situ rather than having undergone ex situ condensation followed by oriented attachment to the melilite inclusion. If the latter had occurred, a uniform distribution of grain orientations within the WLR would not be expected. TEM analysis also identified multiple pyroxene grains sharing the same  $[120]$  orientation (Fig. 3.5c-d), which shows that oriented growth occurs at depth. These data suggest that island-type growth also occurred in three-dimensions for the pyroxene layer in AX30. The data are interpreted in a similar way to TS25, with WLR grains nucleating with similar orientations on preexisting defects in an island growth process. As with TS25, defects in the

melilite inclusion could serve as seed nuclei. In a TEM study by Greshake et al. (1998) they described a high density of dislocations in melilite from CTAs in CV3 chondrites, which lends credence to this hypothesis.

It has been suggested that FTAs are nebular condensates, whereas CTAs experienced at least partial melting at some point in their history. The origins of the WLRs that surround these CAIs also involved high-temperature events in the early solar nebula. WLR formation via condensation, flash heating, and reaction with a nebular gas, or some combinations of these have been suggested (MacPherson et al., 1981; Ruzicka 1997; Wark and Boynton, 2001; Wark and Lovering, 1977; Simon et al., 2005). Further, there is evidence that water was involved in secondary alteration of the Allende parent body (Rowe et al., 1994; Krot et al., 1995; Choi et al., 2000). The microstructural data presented here are consistent with a condensation origin for the WLRs in TS25 and AX30. Nevertheless, it is worth briefly exploring whether transient heating or secondary processing could have affected the microstructure of these inclusions and the WLRs that surround them.

The fine-grained microstructure in the WLR of Axtell could reflect rapid solidification that may have limited solid-state diffusion and thus the ability of the grains to equilibrate. Greenwood (2004) demonstrated that the melting of melilite is kinetically favored relative to other CAI mineral phases. Thus, moderate heating events in the nebula may have preferentially melted this phase. The short duration and moderate temperatures would leave other phases unmelted and, thus, largely unaffected. Therefore, it is possible that the CTA in AX30, even if partially melted at one point in its history, could still preserve the orientations in the pyroxene rim layer.

Analytical studies to resolve excess  $^{26}\text{Mg}$  in the low Al/Mg phases characteristic of WLRs have shown that the high temperature processes occurred several thousands of years after CAI

formation (Simon et al., 2005; Taylor et al., 2005), and Cosarinsky et al. (2005) reports that rim formation occurred over a period of  $\sim 2 \times 10^5$  years. In light of this, the orientations observed here may be the result of a two-step process, where the melilite inclusion is melted and solidifies into a round morphology followed by some transient heating event that later vaporized the outer part of the melilite followed by condensation to form the WLR. Numerous short heating events may have occurred in the early Solar System (Young et al., 2005) that could be responsible for this later melting of the WLR assemblage. Therefore, modification of melilite prior to WLR formation could have occurred in such a way that the CAI/melilite core became a favorable surface on which the WLR could condense.

Refractory inclusions in primitive CV chondrites have been shown to contain Fe- and alkali-rich secondary phases resulting from metasomatic alteration (Kimura and Ikeda, 1997; Krot et al., 2002) as well as phyllosilicates and other hydrated phases resulting from aqueous processing (Tomeoka and Buseck, 1986; Lee and Greenwood, 1993). However, I did not observe sheet silicates or alkali-rich alteration phases in either the FIB or thin sections. Thus, alteration of these samples, if it occurred at all, did not affect the microstructure observed here. Thus, the grain orientations appear to be primary.

Oriented island-type growth therefore appears to be a common mode of formation for the pyroxene in these two WLRs from a CTA and an FTA from oxidized CV3 chondrites. That part of the anorthite layer is also oriented with respect to the pyroxene suggests that subsequent growth of the overlying layers were likely affected by the orientation of the initial condensing material. Moreover, the DFT calculations indicate that such oriented growth is an energy-minimized process. Previous TEM observations revealed clusters of oriented grains within the pyroxene layer of a WLR in the Vigarano CV3 chondrite (Zega et al., 2010). Based on our work

here and those previous results, I hypothesize that preferred orientation may be a common energy-minimized growth mode for grains within the WLRs of CV3 chondrites.

### **3.5 CONCLUSIONS**

I carried out a detailed microstructural study of the WLRs in a CTA from Axtell (AX30) and an FTA from Allende (TS25), reduced and oxidized CV3 chondrites, respectively. EBSD and TEM analyses show the presence of a preferred orientation on the surface of the WLR assemblages as well as at depth in both samples. Clusters of pyroxene grains have common orientations to one another in both TS25 and AX30 and an epitaxial relationship occurs among grains within diopside and anorthite layers in TS25. I conclude that the microstructure of the WLR in TS25 and AX30 is the result of high-temperature condensation of individual grains from a nebular gas, followed by island-type growth into oriented aggregates to form the WLR layers. Regardless of the parent-body histories of TS25 or AX30, the oriented growth of the clusters of grains within their WLRs was preserved. The data suggest that oriented nucleation may be a common growth mode for mineral grains within the WLRs of CV3 chondrites.

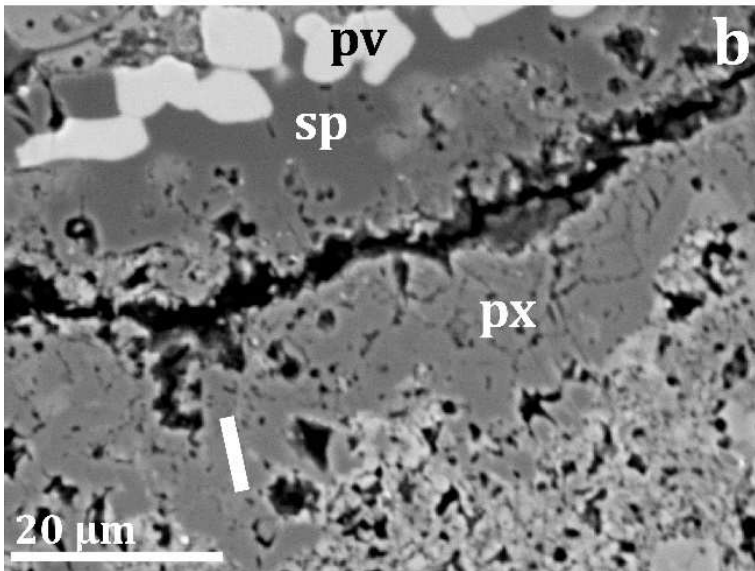
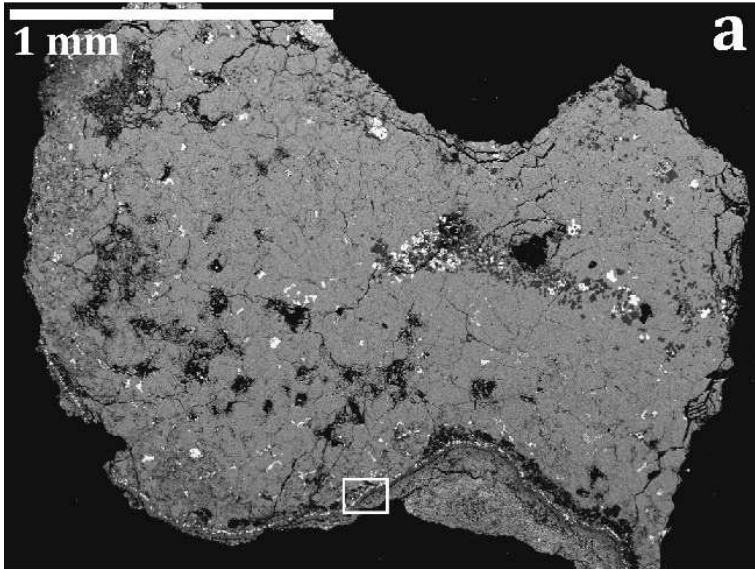


Fig. 3.1 Microprobe data from the Axtell CV3 chondrite. (a) Backscattered electron image of a compact type A CAI. (b) Backscattered electron image of a region of interest for EBSD analysis from the area indicated in (a). The WLR consists of perovskite (pv), spinel (sp), and pyroxene (px). The white bar indicates the location where a FIB section was extracted for TEM analysis.

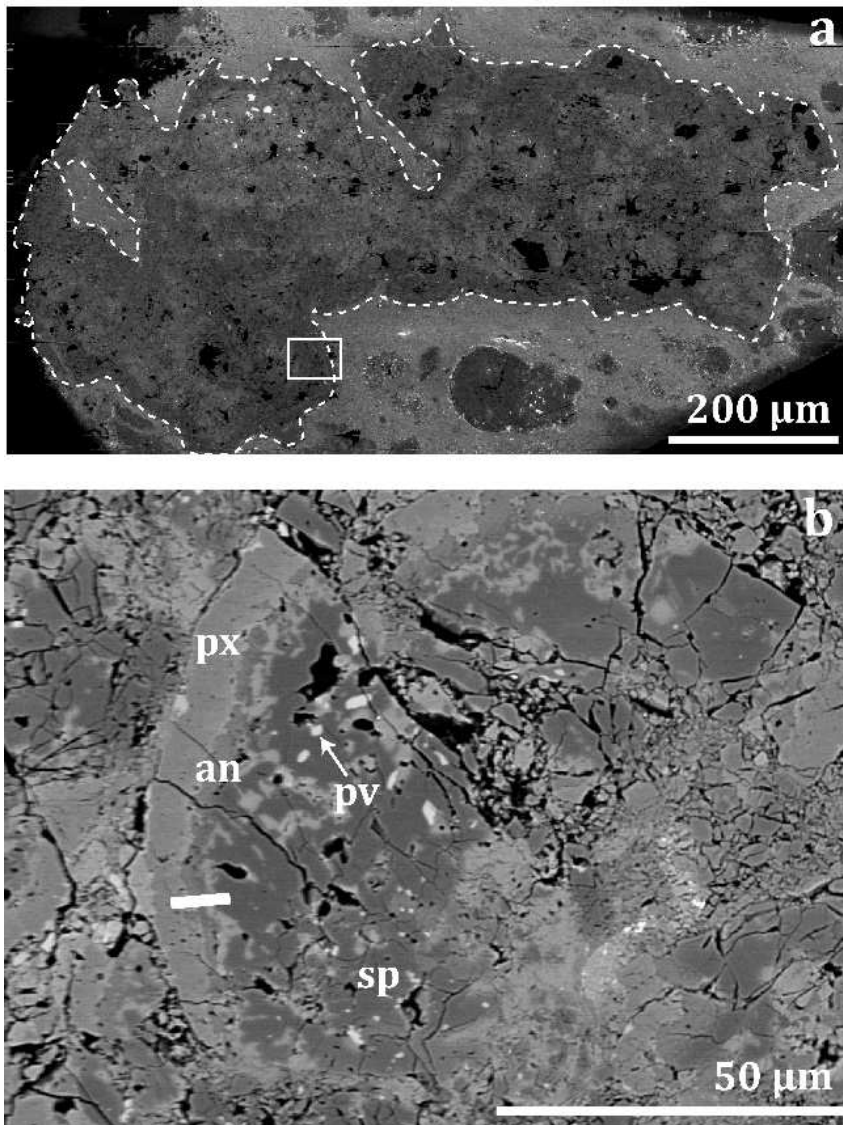


Fig. 3.2 Microprobe data from the Allende CV3 chondrite. (a) Backscattered electron image of a fluffy type A CAI. (b) Backscattered electron image of a region of interest for EBSD analysis from the area indicated in (a). The WLR consists of perovskite (pv), spinel (sp), anorthite (an) and pyroxene (px). The white bar indicates the location where a FIB section was extracted for TEM analysis.

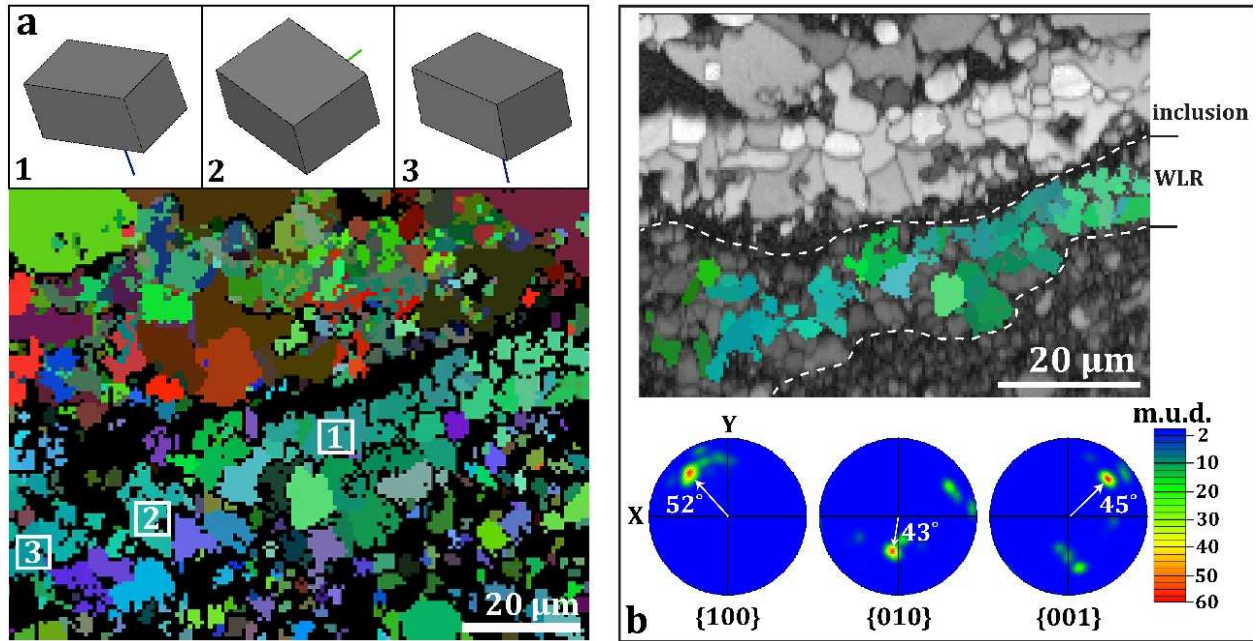


Fig. 3.3 EBSD data on from AX30. (a) Euler map showing the orientations of augite crystals within the WLR from the indicated locations. Primary crystallographic axes are indicated by red (a-axis), green (b-axis), and blue (c-axis) lines. Similar colors indicate similar grain orientations. (b) Grain contrast map of AX30 overlaid with Euler orientations of augite. The {100}-, {010}-, and {001}-pole figures for the grains are shown below. Clusters of grains with similar orientations plot as hotspots within the pole figures. The white arrows represent the angular distribution of the grains from the pole.

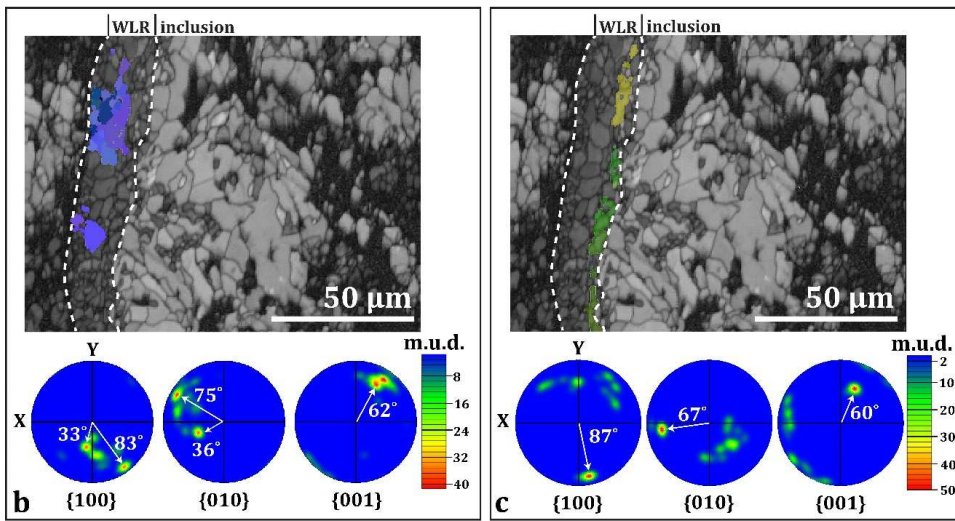
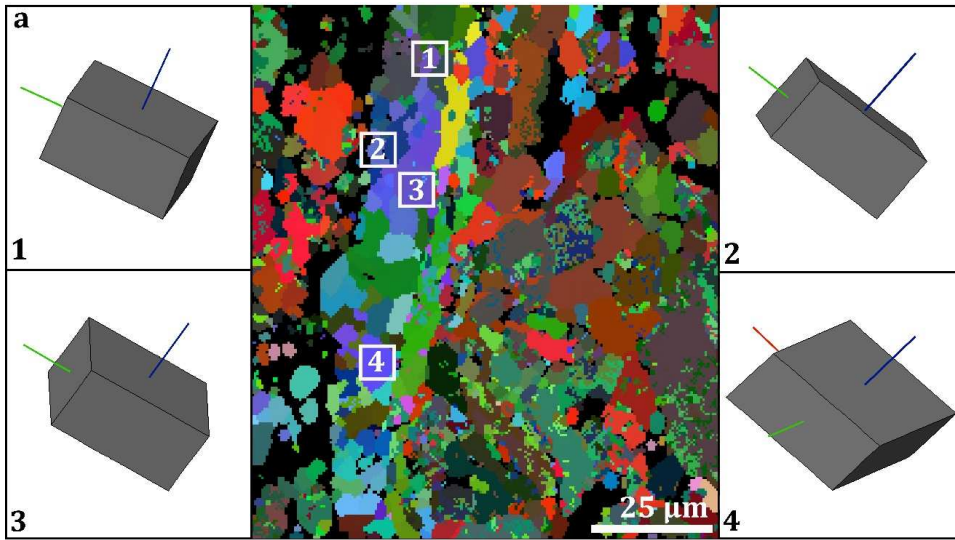


Fig. 3.4 EBSD data on from TS25. (a) Euler map showing the orientations of diopside crystals within the WLR from the indicated locations. Primary crystallographic axes are indicated by red (a-axis), green (b-axis), and blue (c-axis) lines. Similar colors indicate similar grain orientations. (b) Grain contrast map overlaid with Euler orientations of diopside. The {100}-, {010}-, and {001}-pole figures for the grains are shown below. The white arrows represent the angular distribution of the grains from the pole. (c) Grain contrast map overlaid with Euler orientations of anorthite. The {100}-, {010}-, and {001}-pole figures for the grains are shown below. Clusters of grains with similar orientations plot as hotspots within the pole figures. The white arrows represent the angular distribution of the grains from the pole.

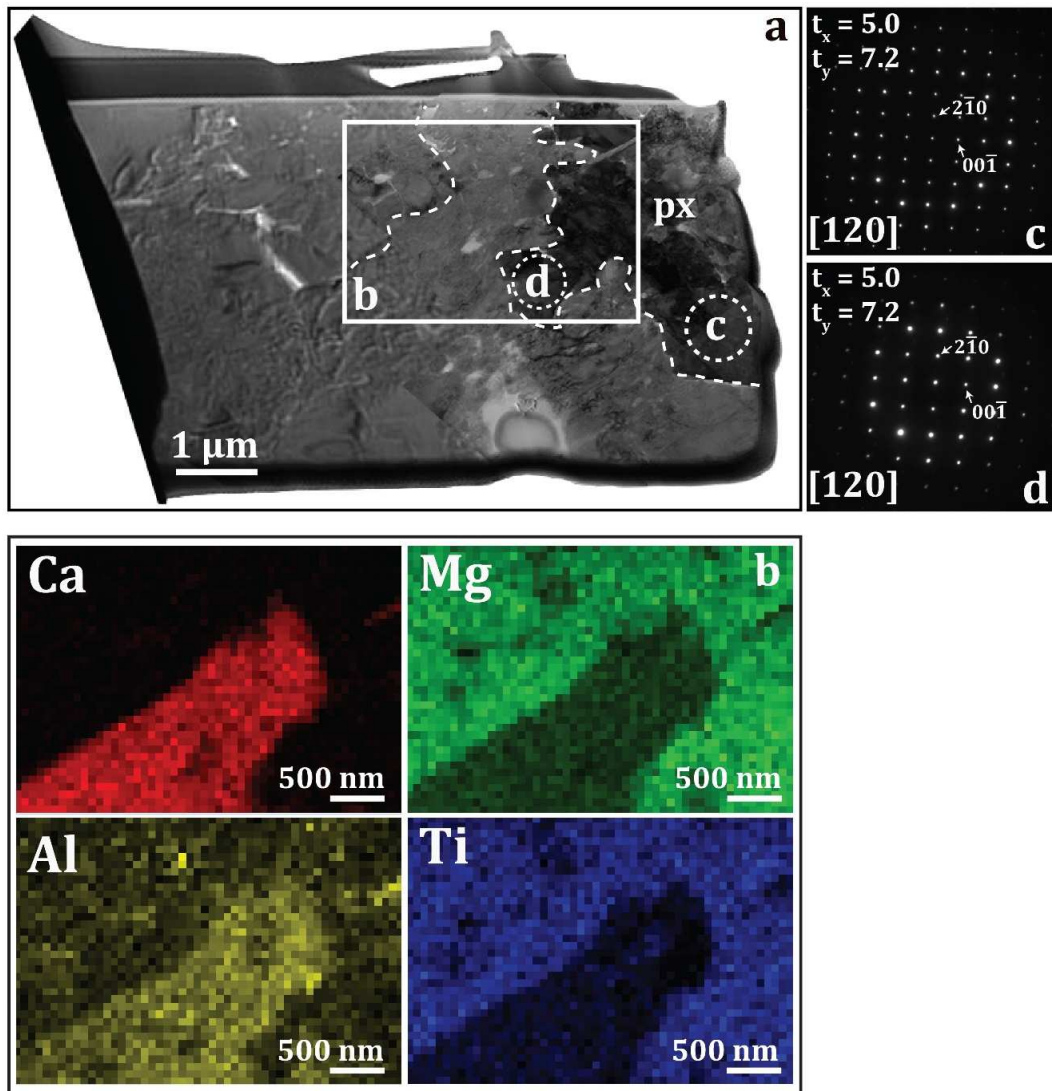


Fig. 3.5 TEM data on a FIB section of AX30 traversing the WLR where EBSD detected the presence of a preferred orientation on the surface, as shown in Fig. 3.1b. (a) Bright-field STEM image comprised of pyroxene (px); (b) EDS maps from the region outlined by a rectangle in (a); (c-d) SAED patterns of orthopyroxene [120] acquired from regions indicated by white-dashed circles in (a). Patterns b and c were acquired at the same goniometer tilt angles ( $t_x$ ,  $t_y$ ).

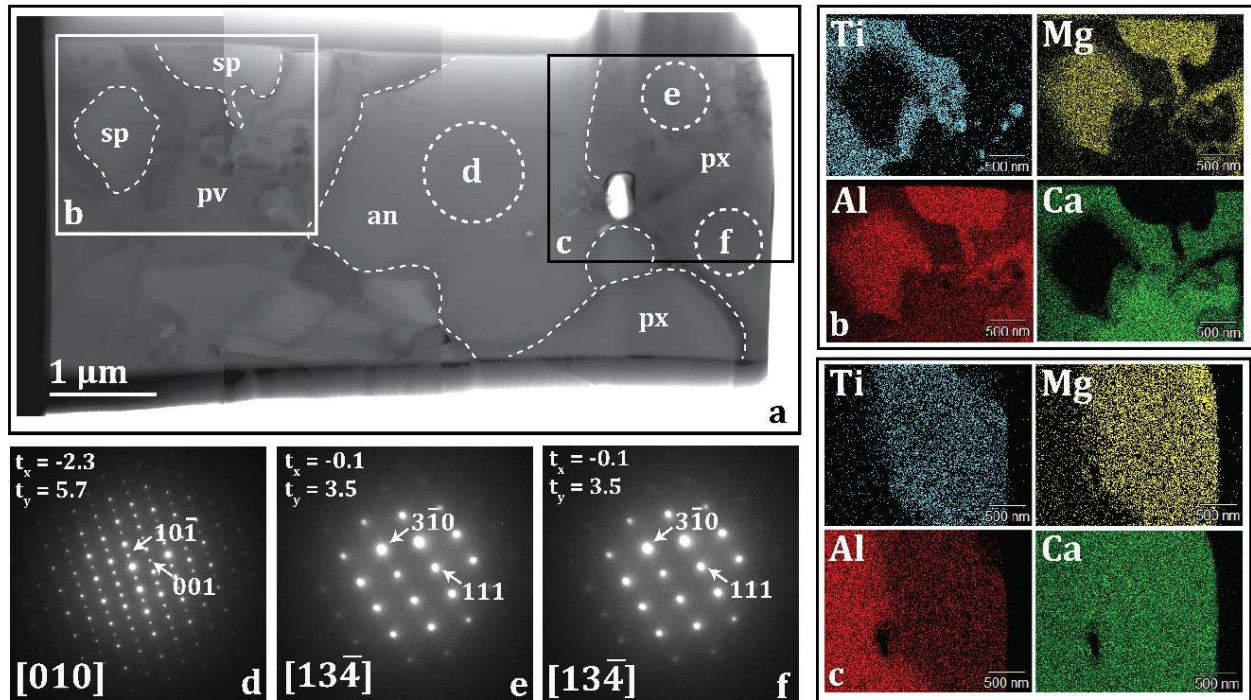


Fig. 3.6 TEM data on a FIB section of TS25 traversing the WLR where EBSD detected the presence of a preferred orientation on the surface, as shown in Fig. 3.2b. (a) Bright-field TEM image comprised of perovskite (pv), spinel (sp), anorthite (an), and pyroxene (px); (b-c) EDS maps from regions outlined by rectangles in (a). (d) SAED pattern of anorthite [010] acquired from region indicated by white-dashed circle in (a); (e-f) SAED patterns of diopside [13-4] acquired from regions indicated by white-dashed circles in (a). Patterns e and f were acquired at the same goniometer tilt angles ( $t_x$ ,  $t_y$ ).

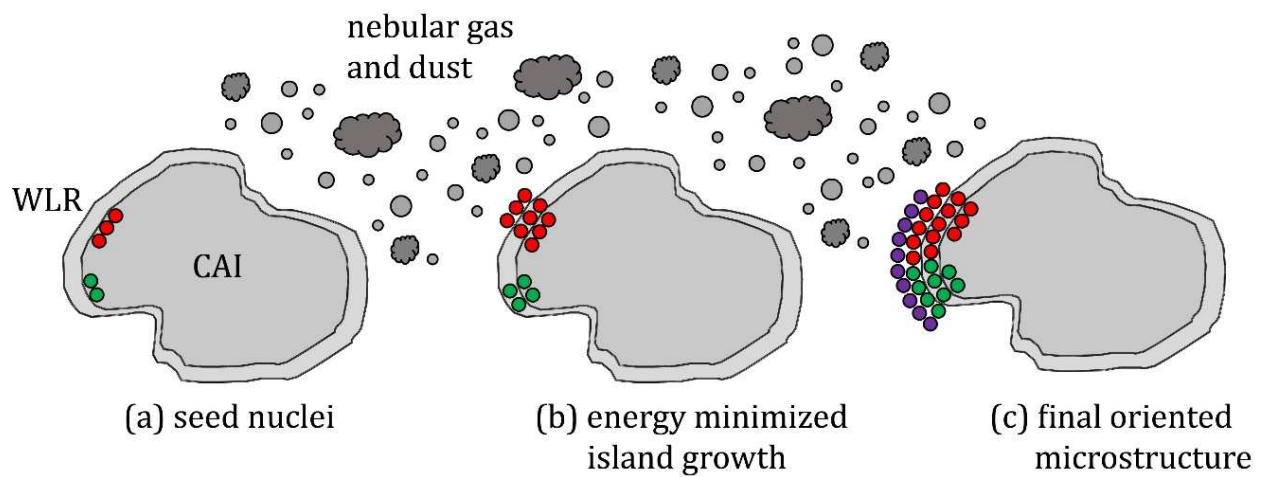


Fig. 3.7 Schematic model depicting WLR growth whereby crystals condense in an oriented fashion onto the CAI surface in order to lower their surface free energy. (a) Grain nucleation occurs when new crystals, represented by colored circles, form on pre-existing seed nuclei. (b) Crystallization of the WLR layers may have occurred at several different nucleation sites via an island-type growth mode. (c) As material condensed from the nebular gas and dust and the WLR grew in size, these grain islands would have merged together creating the observed

## CHAPTER 4

### DEVELOPMENT OF A $fO_2$ BAROMETER

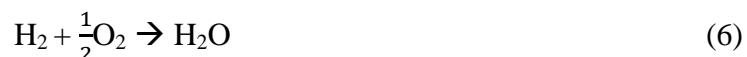
Planetary materials contain an abundance of  $3d$  transition metals. Such metals occur in mineral phases that formed in a wide range of environments including the gaseous envelopes surrounding ancient stars, the solar protoplanetary disk, and meteorite parent bodies. The ability of transition metals to occur in multiple oxidation states makes them potentially useful recorders of the equilibrium partial pressure of oxygen, or oxygen fugacity ( $fO_2$ ), of the nebular gas with which the assemblage may have equilibrated. In this work, an experimental calibration of the relationship between  $fO_2$  and Ti oxidation state in synthetic perovskite is determined. In future work, this calibration will be used to infer the concentration of  $Ti^{3+}$  in meteoritic perovskite. Such measurements are fundamental to quantifying the redox conditions under which planetary materials formed and could be applied to characterizing returned samples from current and future missions, e.g., Stardust (Chi et al., 2009) and OSIRIS-Rex.

#### 4.1 INTRODUCTION TO OXYGEN FUGACITY

In chemical thermodynamics, the oxygen fugacity is equivalent to the partial pressure of oxygen albeit corrected for the non-ideal character of the gas:

$$fO_2 = \gamma PO_2 \quad (5)$$

where  $\gamma$  is the fugacity coefficient and  $PO_2$  is the partial pressure of the gas.  $fO_2$  in the solar nebula is largely determined by the relative abundances of carbon, oxygen, and hydrogen in cosmic gases. The most abundant element in the solar system is overwhelmingly hydrogen (Lodders, 2003). As a result,  $fO_2$  is controlled by the chemical equilibria between water vapor and molecular hydrogen (Rubin et al., 1988):



$$\log f_{\text{O}_2} = 2\log\left(\frac{X_{\text{H}_2\text{O}}}{X_{\text{H}_2}}\right) + 5.67 - 25,664/T \quad (7)$$

Chemical equilibrium calculations show that CAIs formed at high temperatures in a very reducing ( $\log f_{\text{O}_2} \approx -18$ ) region of the protoplanetary disk (Palme and Fegley, 1990; Yoneda and Grossman, 1995; Ebel and Grossman, 2000).

## 4.2 LABORATORY SYNTHESIS OF PEROVSKITE

Perovskite ( $\text{CaTiO}_3$ ) is the second phase after corundum that is thermodynamically predicted to condense from a gas of solar composition (Ebel, 2006). Perovskite containing multivalent Ti is known to occur in CAIs (Simon et al., 2007) and synthetic forms ( $\text{BaTi}_{1-x}\text{NbO}_3$ ; Shao et al., 2010). The redox states of the metal should reflect the  $f_{\text{O}_2}$  and T conditions when the materials formed or last equilibrated. Given the range of conditions potentially experienced by CAIs, such as condensation, large-scale radial transport, and hydrothermal alteration in nebular and parent body environments (Keller and Buseck, 1991; Krot et al., 1995; Brownlee et al., 2006), it is important to quantify the effects of  $f_{\text{O}_2}$  and T on CAI mineral phases. The ratios of  $\text{Ti}^{3+}$  to  $\text{Ti}^{4+}$  in clinopyroxene (Stolper et al., 1982; Beckett and Grossman, 1986), rhönite (Beckett et al., 1986) and hibonite (Beckett et al., 1988) have been used as indicators of oxygen fugacity in CAIs. Based on the successful application of multivalent Ti as an indicator of  $f_{\text{O}_2}$  in those oxides, I hypothesize that other CAI phases such as perovskite could similarly be used as a barometer of nebular  $f_{\text{O}_2}$  conditions.

Perovskite was synthesized by mixing equal amounts of phase-pure oxides CaO (99.995%) and  $\text{TiO}_2$  (99.99%). The synthesis procedure followed a conventional solid-state reaction whereby the raw powders were placed in a Pt crucible that was suspended at the end of an alumina rod in a Deltech vertical tube furnace. The temperature of the furnace was brought to  $1500^\circ\text{C}$  in  $2^\circ\text{C}/\text{min}$  steps over a period of several hours, isothermally held for 2 to 3 days, then

rapidly quenched in water. The sintered powders were ground by hand with ethanol using a mortar and pestle. This process was repeated multiple times until a stoichiometric product was obtained, as verified by electron microprobe (§2.5).

Equilibration experiments were performed at 1 atm in a Deltech vertical tube furnace with an alumina muffle tube that is capable of reaching temperatures of up to 1600°C (Fig. 4.1). The furnace accommodates a Yokogawa UP550E temperature controller, a SiRO2 C700+ solid zirconia electrolyte oxygen sensor, and type-R thermocouple (Pt-Pt<sub>87</sub>Rh<sub>13</sub>). The thermocouple was calibrated against the melting points of various metals including Ag (961°C), Au (1063°C), and Cu (1085°C). The oxygen sensor was calibrated by heating ultra-high purity Fe foil at a  $fO_2$  approximately 0.1 log units above and below the iron-wüstite buffer reaction:



Above the buffer curve, the Fe foil should react to form wüstite. The  $fO_2$  is controlled with a precision of  $\leq 0.5$  log units by way of a gas-mixing system that incorporates a series of mass-flow controllers, specific to the gaseous species of interest, and a chamber containing borosilicate glass for turbulent mixing of the reactive gases prior to their entry into the furnace. For these experiments, the  $fO_2$  was controlled with high purity CO/CO<sub>2</sub> mixtures. The sintered perovskite powders were pressed into pellets, and those experimental charges were subjected to T and  $fO_2$  conditions appropriate to the thermodynamic stability fields for perovskite. The samples were contained in a Pt crucible and suspended in the hot zone by means of a thin Pt wire.

The thermal profile of the furnace must also be calibrated prior to beginning any experiments. This involves identifying the location of the hot zone inside the furnace. The hot zone, defined as the volume in the furnace chamber where the temperature reaches a maximum, was identified by inserting the thermocouple at a rate of 1 cm every 10 minutes to allow the

sensor to equilibrate. The calibration procedure was started 24 hours after the attainment of set point in order to ensure complete thermal stabilization of the furnace. The hot zone is located 16 cm from the top of the furnace (Fig. 4.2).

### **4.3 DETERMINATION OF TI VALENCE STATES**

To determine the Ti valence state, I employed the white-line ratio method. The white-line ratio technique is an established spectroscopic method for the determination of oxidation states of 3*d* transition metals. It is based on the well-documented shift of X-ray absorption spectra from lower to higher energies as the valence of the metal changes from reduced to oxidized states (Manceau et al., 1992; Garvie et al., 1994; van Aken et al., 1998; Delaney et al., 1998; Stoyanov et al., 2007). Fundamentally, the L<sub>2,3</sub> edge arises due to electronic transitions from 2*p* core levels to empty 3*d* states (de Groot et al., 1990; van der Laan et al., 1992). Contributions such as spin state, site geometry, coordination, quadrupole transitions, and multiple scattering events can affect the near-edge structure of absorption spectra, but the white-line method for Ti is based on that developed by Stoyanov et al. (2007), which uses finite energy windows placed precisely before and after the absorption edge so that effects of structure are minimized (Fig. 4.3).

The white-line ratio method relies on the development of a calibration curve, which relates the L<sub>2</sub>/L<sub>3</sub> intensity ratio ( $I_{L_2}/I_{L_3}$ ) to the oxidation states of phase-pure standards (Ti metal, TiO, Ti<sub>2</sub>O<sub>3</sub>, TiO<sub>2</sub>). This curve can then be applied to perovskite extracted from CAIs in order to infer the  $fO_2$  conditions under which they formed or last equilibrated in the early solar nebula.

#### **4.3.1 APPLICATION TO METEORITIC PEROVSKITE**

The relationship between the thermodynamic properties  $f_{\text{O}_2}$  and  $T$  and the concentration of  $\text{Ti}^{3+}$  and  $\text{Ti}^{4+}$  can be derived by assuming the creation of oxygen vacancies. Oxygen is removed from the lattice in the process described by the reaction:



where  $\text{O}$  represents an oxygen atom in a normal lattice site and  $\text{O}^0$  represents an oxygen vacancy (Beckett et al., 1988). The oxygen vacancy creates a net  $2^-$  charge that must be redistributed in order to maintain charge neutrality. The bulk of that redistribution is expected to occur among the Ti cation sites. Thus, we expect two  $\text{Ti}^{4+}$  atoms to be reduced for every oxygen vacancy. With collaborators, we used DFT calculations to evaluate whether oxygen vacancies can form in perovskite. Electronic behavior is fundamental to probing oxidation state, and DFT is a useful theoretical tool for such an application. Preliminary results verify that such vacancies, if created, should reduce the  $\text{Ti}^{4+}$  to  $\text{Ti}^{3+}$  in proportion to the chemical potential of the system. These calculations lend credence to the hypothesis that oxygen vacancies are created in perovskite within extremely reducing and high temperature environments, such as those in which CAIs are inferred to have formed (Simon et al., 2005; Grossman et al., 2008). I attempted to recreate those conditions in the laboratory by way of a gas-mixing furnace (§4.2).

I measured a combination of synthetic perovskite prepared under controlled conditions and meteoritic perovskite extracted from AX30. The perovskite grain was extracted and thinned to electron transparency with a FIB-SEM using previously described methods (Fig. 4.4). XANES spectra of the Ti  $L_{2,3}$  absorption edges for synthetic perovskites show a chemical shift between the reduced and as-grown perovskites (Fig. 4.5). The reduced sample has an edge onset 0.3 eV lower in energy than the as-grown sample, consistent with a decrease in the oxidation state of Ti atoms. The spectrum of a perovskite grain extracted from a CAI more closely resembles the as-grown sample, suggesting a predominant  $\text{Ti}^{4+}$  component. A partially resolved shoulder on the

second  $L_3$  peak appears in the spectrum of meteoritic perovskite. The cause of this feature has been attributed to distortions in the octahedral coordination environment of Ti atoms (de Groot et al., 1990).

Since there are no signs of low-temperature alteration products in the AX30 inclusion, the perovskite may record high temperature conditions in the solar nebula. Oxidizing conditions could suggest that CAIs evolved from a dust-rich environment (Wood, 1984) so that a substantial quantity of pre-existing solids were vaporized prior to condensation. Reducing conditions comparable to those of a gas of solar composition would suggest that the region of the solar nebula from which CAIs evolved was initially relatively dust-free. In the case of AX30, an absence of detectable  $Ti^{3+}$  places a lower limit on the  $fO_2$  of its formation  $\sim 1$  log unit below the iron-wüstite buffer (8). The commonly accepted explanation for enhancing  $fO_2$  in the solar nebula is rapid vaporization of dust (Ebel and Grossman, 2000). Therefore, it is likely that AX30 passed through a dust-rich region at some point during its evolution.

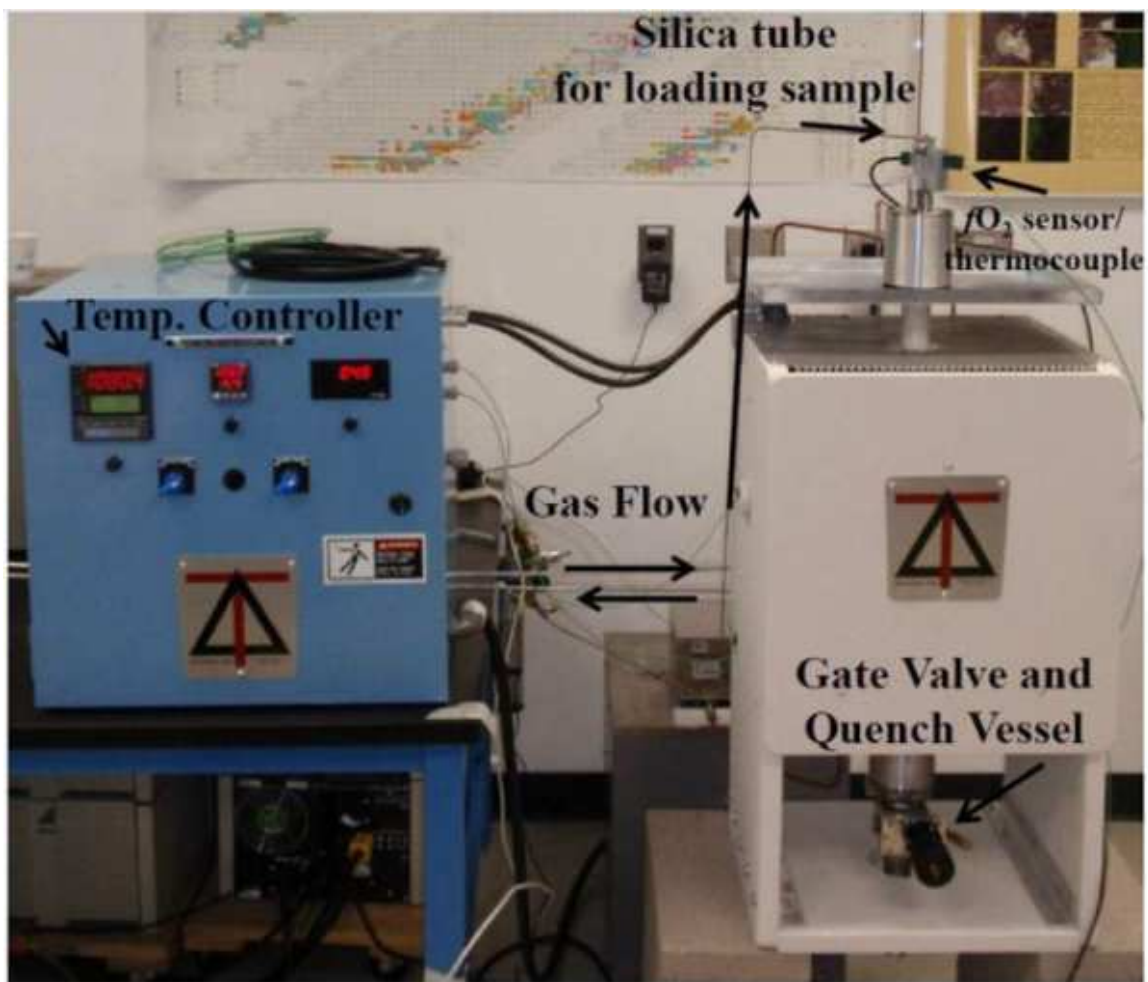


Fig. 4.1 Laboratory set-up for equilibration experiments.

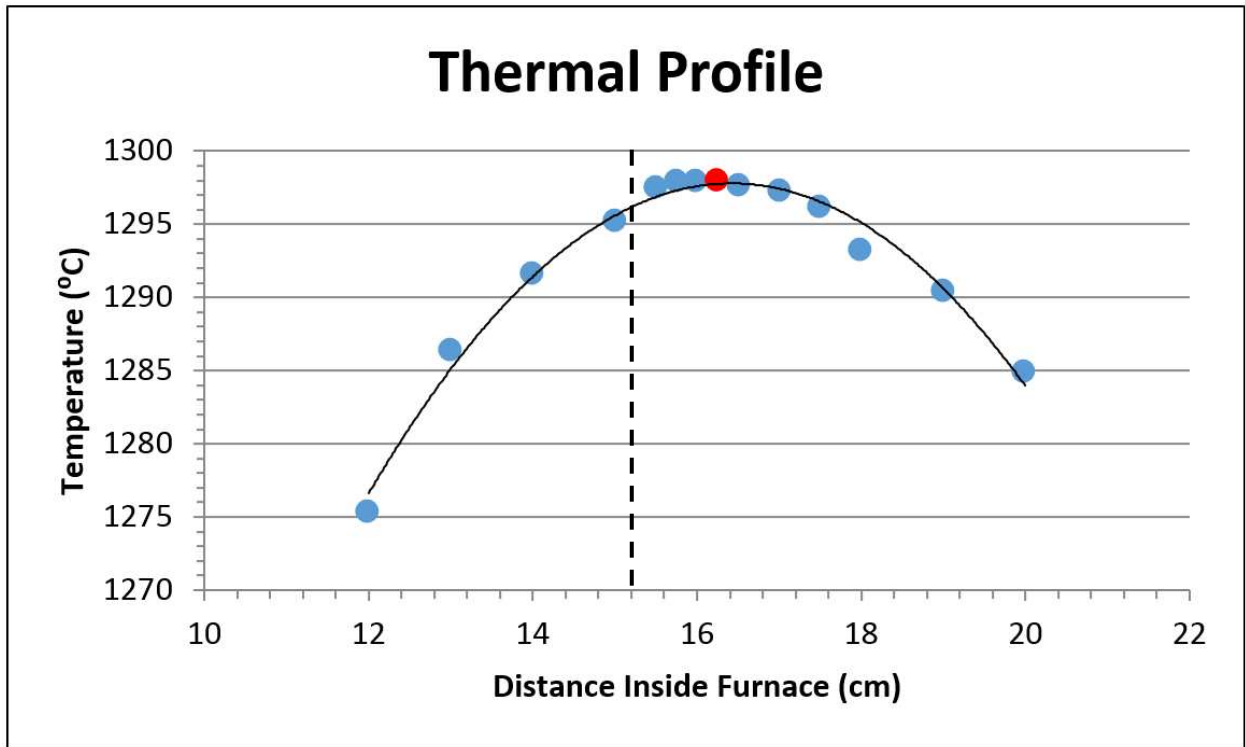


Fig. 4.2 Temperature versus thermocouple position inside the tube. The red dot indicates the position of the hot zone. The dashed line represents the geometric center of the furnace.

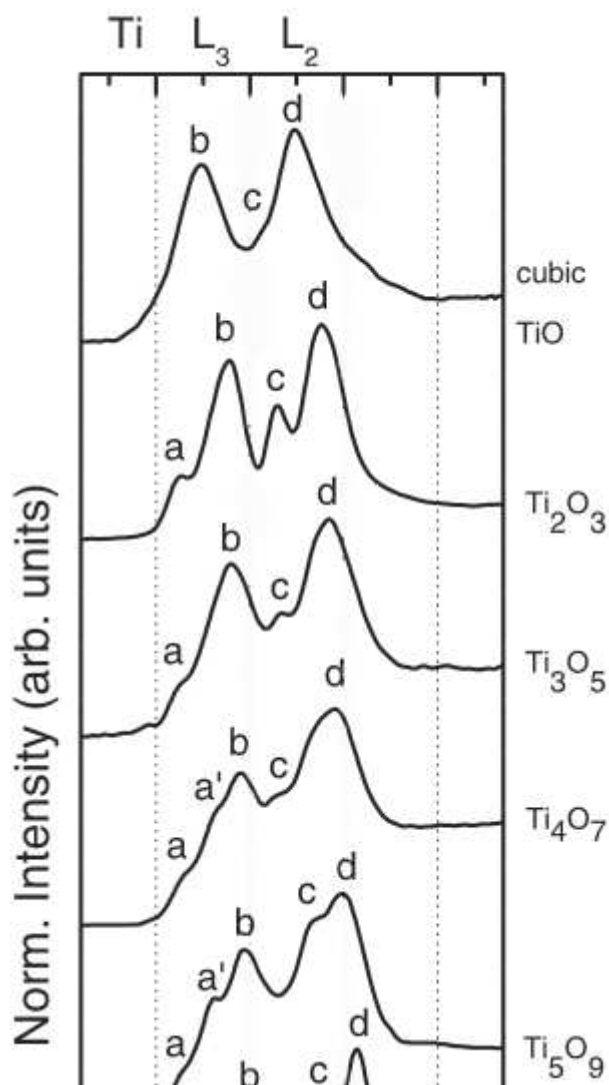


Fig. 4.3 Ti  $L_{2,3}$  electron energy loss near-edge spectra of Ti oxides. The spectra consist mainly of four white lines labeled a, b, c, and d. The valence state of Ti decreases from bottom to top. For the white-line quantification method, integration windows of 1 eV width were centered on the first white line in the  $L_3$  region for  $Ti^{3+}$  and the second white line in the  $L_2$  region for  $Ti^{4+}$ . From Stoyanov et al. (2007)



Fig. 4.4 Bright field TEM image mosaic of a FIB section transecting spinel (sp) and perovskite (pv) in AX30. White dashed lines indicate grain boundaries.

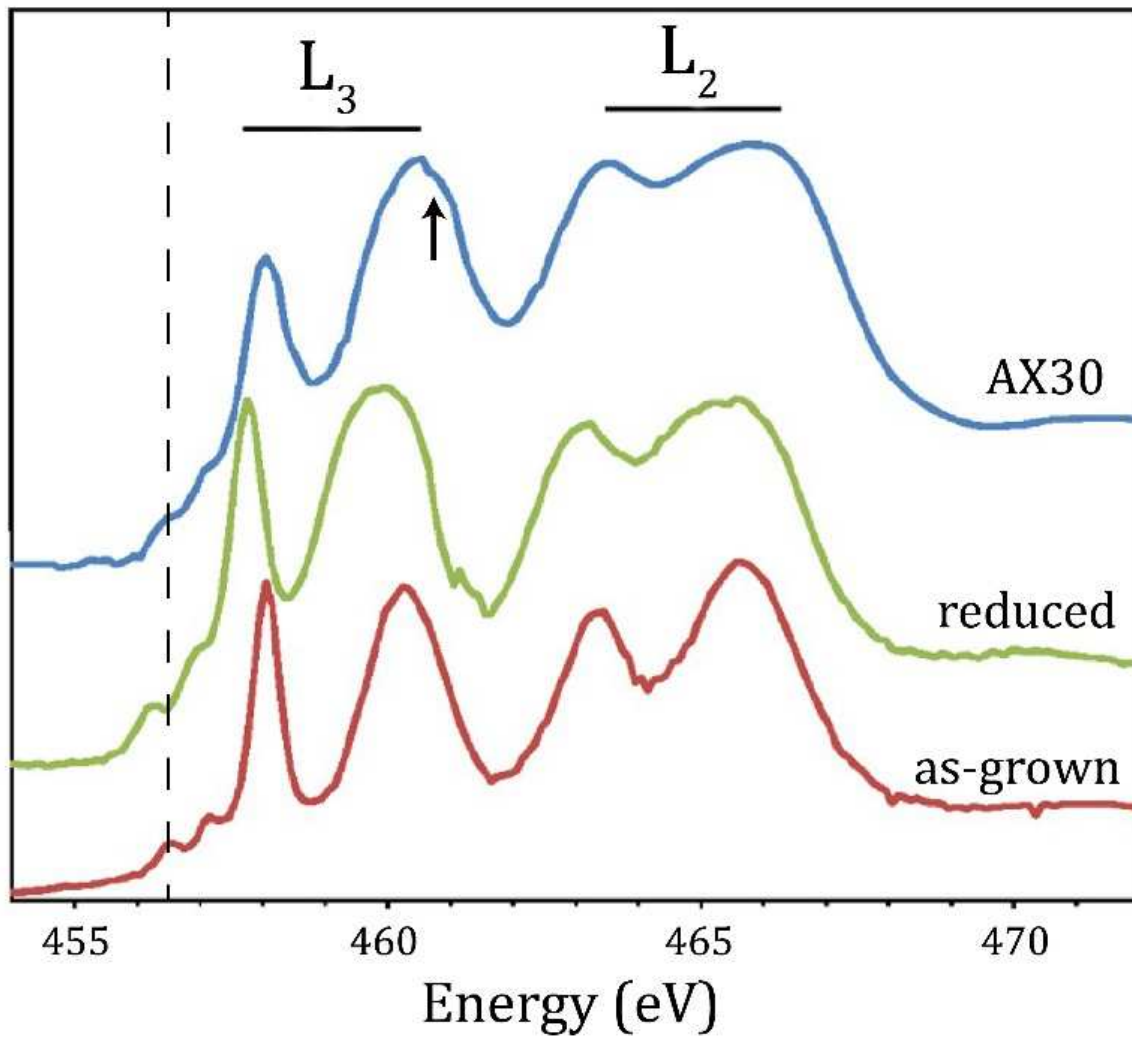


Fig. 4.5 Ti L<sub>2,3</sub> XANES spectra of (top) a perovskite grain extracted from a CAI in Axtell; (middle) synthetic perovskite equilibrated at 1200°C and  $\log f_{\text{O}_2} = -20$  for 121 hours; (bottom) perovskite sintered in air at 1530°C. The dashed line indicates edge onset for the as-grown sample. The arrow highlights a partially resolved shoulder on the second L<sub>3</sub> peak.

## CHAPTER 5

### SUMMARY AND FUTURE WORK

The aim of this thesis has been to investigate the microstructure and crystal chemistry of CAIs and the WLRs that surround them. Through the coordinated application of EBSD, TEM, and XANES enabled by FIB-SEM, I collected comprehensive data sets on the chemical, structural, and electronic properties of FTA and CTA inclusions. There are several lines of research arising from this work that should be pursued. In particular, the work described in Chapter 3 could be extended to include high-resolution TEM (HRTEM) imaging in order to determine the atomic structure and composition at the boundary between WLR layers. HRTEM images, combined with DFT simulations on plausible interfacial structures, could provide additional insights into the formation mechanisms of WLRs. Additionally, the work described in Chapter 4 could be continued with the aim of developing a fully calibrated oxygen barometer. The application of this barometer to additional CAIs should provide useful thermodynamic constraints on dynamical models of the early solar nebula.

## REFERENCES

- Amelin Y., Krot A.N., Hutcheon I.D., Ulyanov A.A. (2002) Lead isotopic ages of chondrules and calcium-aluminum-rich inclusions. *Science* 297, 1678-1683.
- Armstrong J.T., Meeker G.P., Hueneke J.C., Wasserburg G.J. (1982) The Blue Angel: I. The mineralogy and petrogenesis of a hibonite inclusion from the Murchison meteorite. *Geochimica et Cosmochimica Acta* 46, 575-595.
- Barber D.J., Martin P.M., Hutcheon I.D. (1984) The microstructure of minerals in coarse-grained Ca-Al-rich inclusions from the Allende meteorite. *Geochimica et Cosmochimica Acta* 48, 769-783.
- Beckett J.R., Grossman L. (1986) Oxygen fugacities in the solar nebula during crystallization of fassaite in Allende inclusions. 17th Lunar and Planetary Science Conference, 36-37 (abstract).
- Beckett J.R., Haggert S.E., Grossman L. (1986) Origin of  $Ti^{3+}$  bearing rhönite in Ca-Al-rich inclusions: An experimental study. *Meteoritics* 21, 332-333 (abstract).
- Beckett J.R., Live D., Tsay F., Grossman L., Stolper E. (1988)  $Ti^{3+}$  in meteoritic and synthetic hibonite. *Geochimica et Cosmochimica Acta* 52, 1479-1495.
- Beckett, J.R., E. Stolper (1994) The stability of hibonite, melilite and other aluminous phases in silicate melts: Implications for the origin of hibonite-bearing inclusions from carbonaceous chondrites. *Meteoritics* 29, 41-65.
- Beckett J.R., Connolly H.C. Jr., Ebel D.S. (2006) Chemical processes in calcium-aluminum-rich inclusions: A mostly CMAS view of melting and crystallization in: Lauretta D.S., McSween H.Y., Jr. (Eds.), *Meteorites and the early solar system II*. The University of Arizona Press, Tuscon, pp. 399-429.

- Blander M., Fuchs L.H. (1975) Calcium-aluminum-rich inclusions in the Allende meteorite: Evidence for a liquid origin. *Geochimica et Cosmochimica Acta* 39, 1605-1619.
- Brownlee D.E. et al., (2006) Comet 81P/Wild 2 Under a Microscope. *Science* 314, 1711-1716.
- Busemann H., Nguyen A.N., Cody G.D., Hoppe P., Kilcoyne D.A.L., Stroud R.M., Zega T.J., Nittler L.R. (2009) Ultra-primitive interplanetary dust particles from the comet 26P/Grigg-Skjellerup dust stream collection. *Earth and Planetary Science Letters* 288, 44-57.
- Chi M., Ishii H.A., Simon S.B., Bradley J.P., Dai Z., Joswiak D., Browning N.D., Matrajt G. (2009) The origin of refractory minerals in comet 81P/Wild 2. *Geochimica et Cosmochimica Acta* 73 7150-7161
- Choi B.G., Krot A.N., Wasson J.T. (2000) Oxygen isotopes in magnetite and fayalite in CV chondrites Kaba and Mokoia. *Meteoritics and Planetary Science* 35, 1239-1248.
- Cohen, R.E., A.S. Kornacki, and J.A. Wood (1983) Mineralogy and petrology of chondrules and inclusions in the Mokoia CV3 chondrite. *Geochimica et Cosmochimica Acta* 47 1739-1757.
- Cosarinsky M., McKeegan K.D., Hutcheon I.D., Weber P., Fallon S. (2005) Magnesium and oxygen isotopic study of the Wark-Lovering Rim around a fluffy type-A inclusion from Allende. 36<sup>th</sup> Lunar and Planetary Science Conference, #2105 (abstract).
- Cosarinsky M., Leshin L., MacPherson G., Guan Y., Krot A. (2008) Chemical and oxygen isotopic compositions of accretionary rim and matrix olivine in CV chondrites: Constraints on the evolution of nebular dust. *Geochimica et Cosmochimica Acta* 72, 1887-1913.
- Davis A.M., MacPherson G.J., Hinton R.W. (1986) Rims revealed-ion microprobe analysis of individual rim layers in a Vigarano type A inclusion. *Meteoritics* 21, 349-351.
- Davis A.M., MacPherson G.J. (1994) Constraints on the formation of rims on CAIs. *Meteoritics* 29, 458-459.

- de Groot F.M.F., Fuggle J.C., Thole B.T., Sawatzky G.A. (1990)  $2p$  x-ray absorption of  $3d$  transition-metal compounds: An atomic multiplet description including the crystal field. *Physical Review B* 42, 5459-5468.
- Delaney J.S., Dyar M.D., Sutton S.R., Bajt S. (1998) Redox ratios with relevant resolution: Solving an old problem by using the synchrotron microXANES probe. *Geology* 25, 139-142.
- Doukhan N., Doukhan J.C., Poirier J.P. (1991) Transmission electron microscopy of a refractory inclusion from the Allende meteorite: Anatomy of a pyroxene. *Meteoritics* 26, 105-109.
- Ebel D.S., Grossman L. (2000) Condensation in dust-enriched systems. *Geochimica et Cosmochimica Acta* 64, 339-366.
- Ebel, D.S. (2006) Condensation of rocky material in astrophysical environments, in: Lauretta D.S., McSween H.Y., Jr. (Eds.), *Meteorites and the early solar system II*. The University of Arizona Press, Tuscon, pp. 253-277.
- Evans J.W., Thiel P.A., Bartelt M.C. (2006) Morphological evolution during epitaxial thin film growth: Formation of 2D islands and 3D mounds. *Surface Science Reports* 61, 1-128.
- Fagan T.J., Guan Y., MacPherson G.J. (2007) Al-Mg isotopic evidence for episodic alteration of Ca-Al-rich inclusions from Allende. *Meteoritics and Planetary Science* 42, 1221-1240.
- Floss C., Le Guillou C., Brearley A. (2014) Coordinated NanoSIMS and FIB-TEM analyses of organic matter and associated matrix materials in CR3 chondrites. *Geochimica et Cosmochimica Acta* 139, 1-25.
- Garvie L.A.J., Craven A.J., Brydson R. (1994) Use of electron energy-loss near-edge fine structure in the study of minerals. *American Mineralogist* 79, 411-425.
- Giannuzzi, L.A. & Stevie, F.A. 2005 *Introduction to Focused Ion Beams: Instrumentation, Theory, Techniques and Practices*. New York, Springer.

- Goldstein J.I., Newbury D.E., Echlin P., Joy D.C., Fiori C., Lifshin E. Scanning Electron Microscopy and X-Ray Microanalysis. 2nd Ed., Plenum, New York, 1992.
- Graham G.A., Teslich N., Dai Z.R., Bradley J.P., Kearsley A.T., Hörz F. (2006) Focused ion beam recovery of hypervelocity impact residue in experimental craters on metallic foils. *Meteoritics and Planetary Science* 41, 159-165.
- Greenwood R.C., Lee M.R., Hutchison R., Barber D.J. (1994) Formation and alteration of CAIs in Cold Bokkeveld (CM2). *Geochimica et Cosmochimica Acta* 58, 1913-1935.
- Greenwood J.P. (2004) Disequilibrium melting of refractory inclusions: a mechanism for high-temperature oxygen isotope exchange in the solar nebula. *Lunar and Planetary Science* 36, #2132 (abstract).
- Greshake A., Bischoff A., Putnis A. (1998) Transmission electron microscope study of compact Type A calcium-aluminum-rich inclusions from CV3 chondrites: Clues to their origin. *Meteoritics and Planetary Science* 33, 75-87.
- Grossman L. (1972) Condensation in the primitive solar nebula. *Geochimica et Cosmochimica Acta* 36, 597-619.
- Grossman L. (1980) Refractory inclusions in the Allende meteorite. *Annual Review of Earth and Planetary Sciences* 8, 559-608.
- Grossman L., Beckett J.R., Fedkin A.V., Simon S.B., Ciesla F.J. (2008) Redox conditions in the solar nebula: Observational, experimental, and theoretical constraints, in: MacPherson G., Mittlefehldt D.W., Jones J., Simon S.B. (Eds.), Oxygen in the solar system. Mineralogical Society of America, pp. 93-140.
- Heaney P.J., Vicenzi E.P., Gianuzzi L.A., Livi K.J.T. (2001) Focused ion beam milling: A method of site-specific sample preparation for microanalysis of Earth and planetary materials. *American Mineralogist* 86, 1094-1099.

- Hwang R.Q., Bartelt M.C. (1997) Scanning Tunneling Microscopy Studies of Metal on Metal Epitaxy. *Chemical Reviews* 97, 1063-1082.
- Jacobsen C., Wirick S., Flynn G., Zimba C. (2000) Soft X-ray spectroscopy from image sequences with sub-100 nm spatial resolution. *Journal of Microscopy* 197, 173-184.
- Kallemeyn G.W., Rubin A.E., Wasson J.T. (1996) The compositional classification of chondrites: VII. The R chondrite group. *Geochimica et Cosmochimica Acta* 60, 2243-2256.
- Keller L.P., Buseck P.R. (1991) Calcic Micas in the Allende meteorite: Evidence for Hydration Reactions in the Early Solar Nebula. *Science* 252, 946-949.
- Kilcoyne A.L.D., Tyliczszak T., Steele W.F., Fakra S., Hitchcock P., Franck K., Anderson E., Harteneck B., Rightor E.G., Mitchell G.E., Hitchcock A.P., Yang L., Warwick T., Ade H. (2003) Interferometer-controlled scanning transmission X-ray microscopes at the Advanced Light Source. *Journal of Synchrotron Radiation* 10, 125-136.
- Kresse G., Furthmuller J. (1996) Efficiency of ab-initio total energy calculation for metals and semiconductors using plane-wave basis set. *Computational Materials Science* 6, 15-50.
- Kresse G., Joubert D. (1999) From ultrasoft pseudopotentials to the projector augmented-wave method. *Physical Review B* 59, 1758-1775.
- Krot A.N., Scott E.R.D., Zolensky M.E. (1995) Mineralogical and chemical modification of components in CV3 chondrites: Nebular or asteroidal processing? *Meteoritics* 30, 748-775.
- Krot A.N., Hutcheon I.D., Brearley A.J., Pravdivtseva O.V., Petaev M.I., Hohenberg C.M. (2006) Timescales and settings for alteration of chondritic meteorites, in: Lauretta, D.S., McSween, H.Y., Jr. (Eds.), *Meteorites and the early solar system II*. The University of Arizona Press, Tuscon, pp. 525-553.

- Lee M.R., Bland P.A., Graham G. (2003) Preparation of TEM samples by focused ion beam (FIB) techniques: Applications to the study of clays and phyllosilicates in meteorites. *Mineralogical Magazine* 67, 581-592.
- Lodders K. (2003) Solar system abundances and condensation temperatures of the elements. *The Astrophysical Journal* 591, 1220-1247.
- Ma C., Kampf A.R., Connolly Jr H.C., Beckett J.R., Rossman G.R., Sweeney Smith S.A., Schrader D.L. (2011) Krotite,  $\text{CaAl}_2\text{O}_4$ , a new refractory mineral from the NWA 1934 meteorite. *American Mineralogist* 96, 709-715.
- MacPherson G.J., Grossman L. (1979) Melted and non-melted coarse-grained Ca-, Al-rich inclusions in Allende. *Meteoritics* 14, 479-480.
- MacPherson, G.J., Grossman, L., Allen, J.M., Beckett, J.R. (1981) Origin of rims on coarse-grained inclusions in the Allende meteorite. *Geochimica et Cosmochimica Acta Supplement* 16 2, 1079-1091.
- MacPherson G.J., Grossman L. (1984) 'Fluffy' Type A Ca-, Al-rich inclusions in the Allende meteorite. *Geochimica et Cosmochimica Acta* 48, 29-46.
- MacPherson G.J. (2004) Calcium-aluminum-rich inclusions in chondritic meteorites, in: Davis A.M. (Ed.), *Meteorites, Vol. 1, Treatise on Geochemistry*. Elsevier Ltd., Oxford, pp. 201-246.
- Manceau A., Gorshkov A.I., Drits V.A. (1992) Structural chemistry of Mn, Fe, Co, and Ni in manganese hydrous oxides: Part I. Information from XANES spectroscopy. *American Mineralogist* 77, 1133-1143.
- Maranville B.B., Schuerman M., Hellman F. (2006) Simulation of clustering and anisotropy due to Co step-edge segregation in vapor-deposited  $\text{CoPt}_3$ . *Physical Review B* 73, 104435.

- McSween H.Y. (1977) Petrographic variations among carbonaceous chondrites of the Vigarano type. *Geochimica et Cosmochimica Acta* 41, 1777-1790.
- Muller W.F., Wlotzka F. (1982) Mineralogical study of the Leoville meteorite (CV3): Macroscopic texture and transmission electron microscopic observations. *Lunar and Planetary Science Conference XIII*, 558-559 (abstract).
- Nguyen A.N., Nittler L.R., Stadermann F.J., Stroud R.M., Alexander C.M.O'D. (2010) Coordinated analyses of presolar grains in the Allan Hills 77307 and Queen Elizabeth Range 99177 meteorites. *The Astrophysical Journal* 719, 166-189.
- Palme H., Fegley B.J., Jr. (1990) High-temperature condensation of iron-rich olivine in the solar nebula. *Earth and Planetary Science Letters* 101, 180-195.
- Parker S.C., Grant A.W., Bondzie V.A., Campbell C.T. (1999) Island growth kinetics during the vapor deposition of gold onto TiO<sub>2</sub>(110). *Surface Science* 441, 10-20.
- Perdew J.P., Burke K., Ernzerhof, M. (1996) Generalized gradient approximation made simple. *Physical Review Letters* 77, 3865-3868.
- Rubin A., Fegley B.J., Jr., Brett R. (1988) Oxidation state in chondrites, in: Kerridge J.F., Matthews M.S. (Eds.), *Meteorites and the Early Solar System*. The University of Arizona Press, Tuscon, pp. 488-511.
- Ruzicka A. (1997) Mineral layers around coarse-grained, Ca-Al-rich inclusions in CV3 carbonaceous chondrites: Formation by high-temperature metasomatism. *Journal of Geophysical Research: Planets* 102, 13387-13402.
- Ruzicka A. (2012) Mineral layers around coarse-grained, Ca-Al-rich inclusions in CV3 carbonaceous chondrites: Formation by high-temperature metasomatism. *Journal of Geophysical Research* 102, 13387-13402.

- Scott E.R.D., Krot A.N. (2005.) Chondritic meteorites and the high-temperature nebular origins of their components, in: Krot A.N., Scott E.R.D., Reipurth B. (Eds.), Chondrites and the protoplanetary disk. Astronomical Society of the Pacific, San Francisco, pp. 15-53.
- Shao Y., Maunders C., Rossouw D., Kolodiaznyi T., Botton G.A. (2010) Quantification of the Ti oxidation state in  $\text{BaTi}_{1-x}\text{Nb}_x\text{O}_3$  compounds. *Ultramicroscopy* 110, 1014-1019.
- Shchukin V.A., Bimberg D. (1999) Spontaneous ordering of nanostructures on crystal surfaces. *Reviews of Modern Physics* 71, 1125.
- Simon J.I., Young E.D., Russell S.S., Tonui E.K., Dyl K.A., Manning C.E. (2005) A short timescale for changing oxygen fugacity in the solar nebula revealed by high-resolution  $^{26}\text{Al}$ - $^{26}\text{Mg}$  dating of CAI rims. *Earth and Planetary Science Letters* 238, 272-283.
- Simon S.B., Davis A.M., Grossman L. (1999) Origin of compact type A refractory inclusions from CV3 carbonaceous chondrites. *Geochimica et Cosmochimica Acta* 63, 1233-1248.
- Simon S.B., Sutton S.R., Grossman L. (2007) Valence of titanium and vanadium in pyroxene in refractory inclusion interiors and rims. *Geochimica et Cosmochimica Acta* 71, 3098-3118.
- Stoffler D., Keil K., Scott E.R.D. (1991) Shock metamorphism of ordinary chondrites. *Geochimica et Cosmochimica Acta* 55, 3845-3867.
- Stolper E. (1982) Crystallization sequences of Ca-Al-rich inclusions from Allende: An experimental study. *Geochimica et Cosmochimica Acta* 46, 2159-2180.
- Stoyanov E., Langenhorst F., Steinle-Neumann G. (2007) The effect of valence state and site geometry on Ti  $L_{3,2}$  and O K electron energy-loss spectra of  $\text{Ti}_x\text{O}_y$  phases. *American Mineralogist* 92, 577-586.
- Stroud R.M., Nittler L.R., Alexander C.M.O.D. (2004) Polymorphism in presolar  $\text{Al}_2\text{O}_3$  grains from asymptotic giant branch stars. *Science* 305, 1455-1457.

- Taylor D.J., McKeegan K. D., Krot A. N. (2005) High resolution  $^{26}\text{Al}$  chronology: Resolved time interval between rim and interior of a highly fractionated compact type A CAI from Efremovka. 36<sup>th</sup> Lunar and Planetary Science Conference, #2121 (abstract).
- Toppani A., Libourel G., Robert F., and Ghanbaja J. (2006) Laboratory condensation of refractory dust in protosolar and circumstellar conditions. *Geochimica et Cosmochimica Acta* 70, 5035-5060.
- van Aken P.A., Liebscher B., Styrsa V.J. (1998) Quantitative determination of iron oxidation states in minerals using Fe L<sub>2,3</sub>-edge electron energy-loss near-edge structure spectroscopy. *Physics and Chemistry of Minerals* 25, 323-327.
- van der Laan G., Kirkman I.W. (1992) The 2p absorption spectra of 3d transition metal compounds in tetrahedral and octahedral symmetry. *Journal of Physics: Condensed Matter* 4, 4189-4204.
- Van Schmus W.R., Wood J.A. (1967) A chemical-petrologic classification for the chondritic meteorites. *Geochimica et Cosmochimica Acta* 31, 747-765.
- Wark D.A., Lovering J.F. (1977) Marker events in the early solar system: evidence from rims on Ca-Al-rich inclusions in carbonaceous chondrites. 8th Lunar and Planetary Science Conference, 95-112.
- Wark D.A., Boynton W.V. (2001) The formation of rims on calcium-aluminum-rich inclusions: Step I-Flash heating. *Meteoritics and Planetary Science* 36, 1135-1166.
- Wasson J.T. (1985) *Meteorites: Their Record of the Early Solar System History*. Freeman, New York.
- Wood J.A. (1984) On the formation of meteoritic chondrules by aerodynamic drag heating in the solar nebula. *Earth and Planetary Science Letters* 70, 11-26.

- Wood J.A. (1988) Chondritic meteorites and the solar nebula. *Annual Review of Earth and Planetary Sciences* 16, 53-72.
- Yoneda S., Grossman L. (1995) Condensation of CaO-MgO-Al<sub>2</sub>O<sub>3</sub>-SiO<sub>2</sub> liquids from cosmic gases. *Geochimica et Cosmochimica Acta* 59, 3413-3444.
- Zega T.J., Cosarinsky M., Stroud R.M., McKeegan K.D. (2007) FIB-TEM study of a Wark-Lovering rim in an Allende type A CAI. *Meteoritics and Planetary Science* 42, A169.
- Zega T.J., Cosarinsky M., MacPherson G.J., McKeegan K.D. (2009) FIB-TEM analysis on a Wark-Lovering rim from the Vigarano CV3 chondrite. *Meteoritics and Planetary Science* 44, A226.
- Zega T.J., Alexander C.M.O.D., Nittler L.R., Stroud R.M. (2010) The microstructure of a presolar spinel grain. 41<sup>st</sup> Lunar and Planetary Science Conference, #2055 (abstract).
- Zega T.J., Simon S.B., Grossman L. (2010) Microstructural analysis of a Wark-Lovering rim around an Allende CAI. *Meteoritics and Planetary Science* 45, A223.
- Zolensky M.E., Barrett R., Browning L. (1993) Mineralogy and composition of matrix and chondrule rims in carbonaceous chondrites. *Geochimica et Cosmochimica Acta* 57, 3123-3148.